CORE SAMPLE CHARACTERISATION USING 3D TERRESTRIAL LASER SCANNING | TU DELFT

Supervisors: Dr. R.C. Lindenbergh (TU Delft)
Dr. B. Meijninger (Fugro)

Applied Earth Sciences | Bachelor Thesis | I.E. van Berkom
July 2017

ABSTRACT

The main purpose of this thesis is to conclude whether terrestrial laser scanning (TLS) can be used as an automated method to improve the classification of soils. It was in collaboration with Fugro N.V., a large Dutch consultancy and engineering firm that is active in onshore and offshore services in the field of geological and geotechnical investigations for a wide field of clients in the petroleum and gas industry but also for other infrastructure. Current methods for the classification of soils comprise of laboratory and in-situ measurements. Fugro is searching for a more accurate and time efficient method to classify soil and provided five core samples on which a classification had to be performed. The Leica C10 laser scanner, provided by the department of Geoscience and Remote Sensing (TU Delft), was used to scan the soil samples. TLS is based on LIDAR (light detection and ranging) which is known for emitting pulses in a very narrow beam of monochromatic light (one wavelength) in the ultraviolet, visible or near-infrared range of the electromagnetic spectrum. After scanning the core samples, the following features extracted from the 3D point cloud data were used to perform classification on each core sample: intensity (backscattered energy), colour (an RGB-image), surface height variations (roughness). The chosen method was iso cluster unsupervised classification. After classification, interpretations were made based on the descriptions of the core sample and knowledge of bare soil reflectance. The main factors that influenced the soil reflectance were related to characteristics of the samples: glauconite content (an iron-bearing mineral) and surface roughness. Both factors were responsible for a decrease in soil reflectance. Unsupervised classification was applicable on three out of five samples. However, only one sample provided good results. The other two samples were less promising, although some features could clearly be identified after comparing the classified image with ground truth data.

PREFACE

This thesis report was written to obtain my Bachelor's Science degree in Applied Earth Sciences at Delft University of Technology. I would like to thank my supervisors Dr. R.C. Lindenbergh (TU Delft) for guiding me through my thesis and to keep me on the academic path and Dr. B. Meijninger (Fugro) whose enthusiasm helped me pursuing this research, for his prompt replies to my requests and in particular for the quick delivery core samples which jumpstarted my research. This thesis helped me broaden my interest in both fields of Remote Sensing and Geo-Engineering.

I.E. van Berkom

Delft, July 2017

CONTENTS

1. INTRODUCTION

Assessing the response of civil constructions to movements in the subsurface requires thorough knowledge of soil behaviour in the subsurface. One of the potential negative impacts of earthquakes is liquefaction, described by the behaviour of water-saturated loose sand and silt as a liquid after stress is applied (U.S. Geological Survey, 2006). When liquefaction occurs in the subsurface, buildings and dikes will most likely experience large stability problems. Therefore, it is of great importance that this phenomenon is understood. The integration of soil mechanics and geology is essential in this study. Fugro N.V., a large Dutch consultancy engineering firm, active in the field of onshore and offshore, provides geological and geotechnical investigations for the wide field of clients in the petroleum and gas industry but also for infrastructure. Characterisation of soils from core logging can be very time consuming. While several visual and laboratory methods for the classification of soils currently exist, Fugro seeks for a method that is less time consuming and that has a higher accuracy.

One of the applications of laser scanning is to extract information from the topography of the surface. Although no evidence has been found of the classification of core samples using laser scanning technology, theoretically this method should work. Each point of a raw 3D point cloud dataset from laser scanning consists of an X, Y and Z position (the topography of the soil surface), RGB values (an image) and intensity values (the amount of backscattered energy). This information can be used to describe certain characteristics of a soil bedding and be used for the classification of soil.

In this thesis, the research question states whether terrestrial laser scanning (TLS) can be used as an automated method to improve core sample classification. To provide an appropriate answer, several sub-questions are formulated:

- What are the advantages of this method compared to the current (in-situ and laboratory) methods?
- Can classification using TLS be performed on all core samples and how reliable are the results?
- For what core samples can this method be used and for what applications is it not suitable?
- What factors influence the classification result of a core sample and how? What factor is the largest contributor and why?

2. THE CORE SAMPLES

Fugro has provided five core samples on which laser scanning will be tested. The samples were taken from different depth intervals of borehole B508 – 4 near Terneuzen (province Zeeland, the Netherlands). It was part of a project where a new lock had to be constructed from the canal of Terneuzen to Belgium. The samples are part of geotechnical unit E which is interpreted as the Tongeren Formation (Fugro Engineers B.V., 2015). The Tongeren Formation is a geological formation in the Dutch and Belgian subsurface formed during the Upper Eocene to Lower Oligocene, 34 to 37 million year ago, as part of the Middle North Sea Group (Berendsen, 2004). A chronostratigraphic chart can be found in Appendix A. The sediment layers of geotechnical unit E were deposited on a shelf during a shallow marine environment. They consist of fine sands and are interbedded with silty sands, locally with thin to medium beds of sandy clay (Fugro Engineers B.V., 2015). A notable characteristic is the substantial amount of glauconite that is found in the samples.

2.1. Glauconite

Glauconite, that has the chemical formula (K, Na)(Fe,Mg,Al)2(Si,Al)4O10(OH)2, is a mineral known for its dark green colour ("glaucos" is the Greek word for "bluish green"). It is formed by clay that weathers in a relatively warm shallow marine environment and is found mainly in silty and sandy layers (van den Bosch, 2015). The colours of glauconite vary from lighter green, in silty clay deposits, to dark green, in sandy deposits. Glauconites in silty clay deposits occur as relatively soft particles, while glauconite particles are harder in sandy deposits (van den Bosch, 2015). Due to the fact that glauconite is made out of clay minerals, it is much softer than quartz (sand) and known for its easy deformation when mechanical stress is applied (van Alboom, Dupont, Maertens, & Haelterma, 2012). The amount of glauconites in a soil is an important factor for the geotechnical characteristics and behaviour of the soil.

Another important characteristic of glauconite is its high iron content (van Alboom, Dupont, Maertens, & Haelterma, 2012). The iron content in soils is one of the factors that influence the overall soil reflectance (Stoner & Baumgardner, 1981) and thus the intensity value from laser scanning data. General characteristics of soil spectra and its influencing factors is covered in Section 3.

2.2. Layer descriptions

The samples L9, L12, L14, L15 and L19 represent the layers from borehole B508 – 4 (Figure B.1, Appendix B) with intervals: 60.00 – 60.55 m, 63.00 – 63.72 m, 65.00 – 65.75 m, 66.00 – 66.78 m and 70.00 – 70.72 m respectively (Figure 2.2.1). After visual inspection of the core samples together with the layer descriptions that were provided by Fugro (Appendix B), sub-layers for each core sample could be distinguished from each other and classified, as given in Table 2.1.

Table 2.1. Layer descriptions of core samples L9, L12, L14, L15 and L19.

Sample	***Interval (cm)***	***Label***	***Description***
L9	6000 – 6020	Sand	Moderately to very silty
	6020 – 6038	Clay	Extremely silty
	6038 – 6054	Loam[1]	Very sandy
L12	6300 – 6315	Sand	Moderately to very silty
	6315 – 6330	Clayey sand	Strong laminations
	6330 – 6040	Clay	Very sandy
	6040 – 6050	Sand	Moderately to very silty
	6050 – 6070	Clay	Extremely silty
L14	6500 – 6510	Sand	Very silty
	6510 – 6560	Sand	Moderately silty
	6560 – 6570	Clay	Very sandy
	6570 – 6575	Sand	Moderately silty
L15	6600 – 6678	Sand	Moderately silty
L19	7000 – 7072	Sand	Moderately silty

Figure 2.2.1. From left to right: Sample L9, L12, L14, L15 and L19.

[1] A mixture of silt, clay and primarily sand, formed by the compaction and depletion of organic matter (Kaufmann & Cleveland, 2008).

3. LASER SCANNING

Remote sensing is used to sense information from a certain distance ("remotely") (Chuvieco, 2016). It is about the interaction between an object and a sensor, where information about the object is captured. A human eye, for example, is a sensor. When it registers an object, it means that the eye senses the reflected energy from the object that is reflected by an illumination source, the sun for example (solar radiation). Electromagnetic (EM) radiation that is visible to the human eye is *light* (ITC, 2012). In the absent of light, the object would not be sensed or observed by the human eye as it is only sensitive to the visible wavelengths of light. The human eye is limited to a small part of the EM spectrum, approximately 400 – 700 nm. It does not sense other sources of energy, like e.g. the thermal energy (warmth) emitted by a plant. Outside this range, other sensors are used in remote sensing that are able to detect EM radiation.

Before discussing laser scanning, the fundamentals of laser scanning should be considered: electromagnetic radiation. Section 3.1 describes how electromagnetic radiation interacts with objects and how it is used in remote sensing observation. In Section 3.2, an explanation of the main factors that influence the reflectance of soil is given. Section 3.3 discusses the principles and applications of LIDAR. Finally, the laser scanner Leica C10 used for this thesis will be described in Section 3.4.

3.1. Electromagnetic radiation

EM radiation is explained by two theories of light: the wave theory (Maxwell, Huygens) and quantum theory (Planck, Einstein). According to the wave theory, light waves travel through space in a straight line, if not influenced by external factors, with oscillating electric and magnetic components that are orthogonal to each other and to the propagation direction: the velocity of light (Figure 3.1.1). According to the quantum (or particle) theory, EM radiation is explained by discrete packages of energy: photons. A photon carries an amount of energy of a specific wavelength. Combining the two theories yields to the following relation (Chuvieco, 2016):

$$Q = h\left(\frac{c}{\lambda}\right) \tag{3.1}$$

Where:

- Q is the energy of a photon (in joules, J)
- h is Planck's constant ($6.626 \cdot 10^{-34}$ J s)
- c is the constant velocity of light ($3 \cdot 10^{8}$ m/s)
- λ is the wavelength, a measure of the distance between two successive peaks in the same phase (in micrometres, 1 µm = 10^{-6} m or in nanometres, 1 nm = 10^{-9} m)

This equation reveals that the amount of energy is inversely proportional to the wavelength, or proportional to the frequency. Hence, the shorter the wavelength, or the higher the frequency, the higher the amount of energy. Therefore, energy detection of shorter wavelengths is easier than that of longer wavelengths (Chuvieco, 2016).

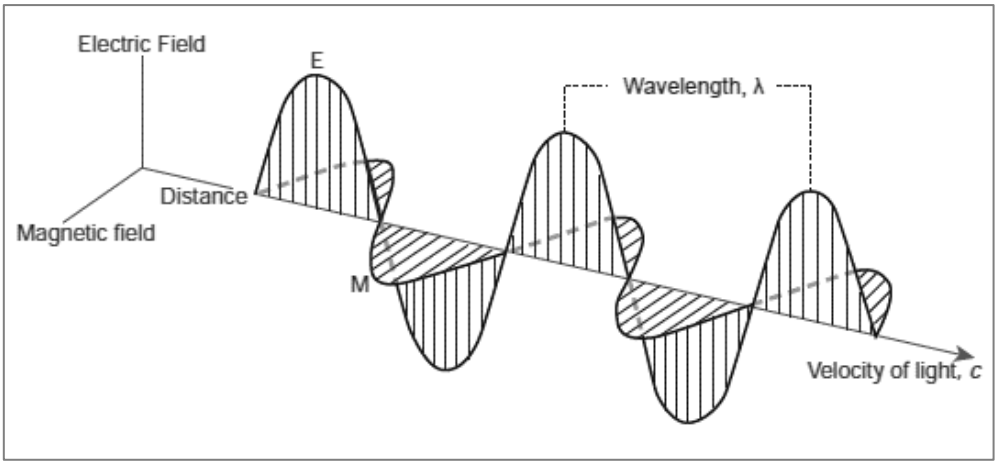

Figure 3.1.1. The oscillating electric and magnetic components of EM radiation as explained by the wave theory of light (ITC, 2012).

Figure 3.1.2 illustrates the wide range of the EM spectrum where names are given to the spectral regions that are frequently used in remote sensing observation. Atmospheric transmittance is high where the blocking effect of the atmosphere is low, as seen in Figure 3.1.2. This effect is explained by gases in the atmosphere (mainly O_2, O_3, H_2O and CO_2) that cause atmospheric absorption (Chuvieco, 2016). Thus, the parts of the EM spectrum (spectral regions) that can be used for remote sensing observation are parts where atmospheric transmittance is high (atmospheric windows) and thus reflectance of objects on the earth surface is high. Only the spectral regions of the optical window will be treated, as the laser scanner that is used for this project is a LIDAR sensor that works in the optical domain. LIDAR will be treated further in Section 3.3.

The visible (VIS) region (0.4–0.7 μm) is divided into three smaller regions: blue (0.4–0.5 μm), green (0.5–0.6 μm) and red (0.6–0.7 μm). These are the spectral wavelengths that can be detected by the human eye. The near-infrared (NIR) region (0.7-1.2 μm) is known for its sensitivity to determine the status of healthy vegetation. The mid-infrared (MIR) region (1.2-8 μm) is known for its ability to give good estimations on the moisture content of vegetation and soil.

When EM radiation interacts with objects of the earth surface, reflection and absorption characteristics of the object can be studied. The amount of reflected radiation is expressed as the ratio of the reflected radiation to the incoming radiation for a certain wavelength (Chuvieco, 2016). The reflectance behaviour over a certain wavelength of the EM spectrum is called a spectral reflectance signature. These reflectance curves are unique for different objects like vegetation, bare soil and water (Figure 3.1.3). Healthy vegetation is known for its typical spectral reflectance curve, where reflectance is lower in the VIS region and very high in the NIR region. The dips at 1.4 and 1.9 μm are typical for vegetation curves and caused by the absorption of water molecules in the atmosphere. Soil reflectance is much less affected by these water absorption peaks, as can be noticed from spectral reflectance curve for soil in Figure 3.1.3.

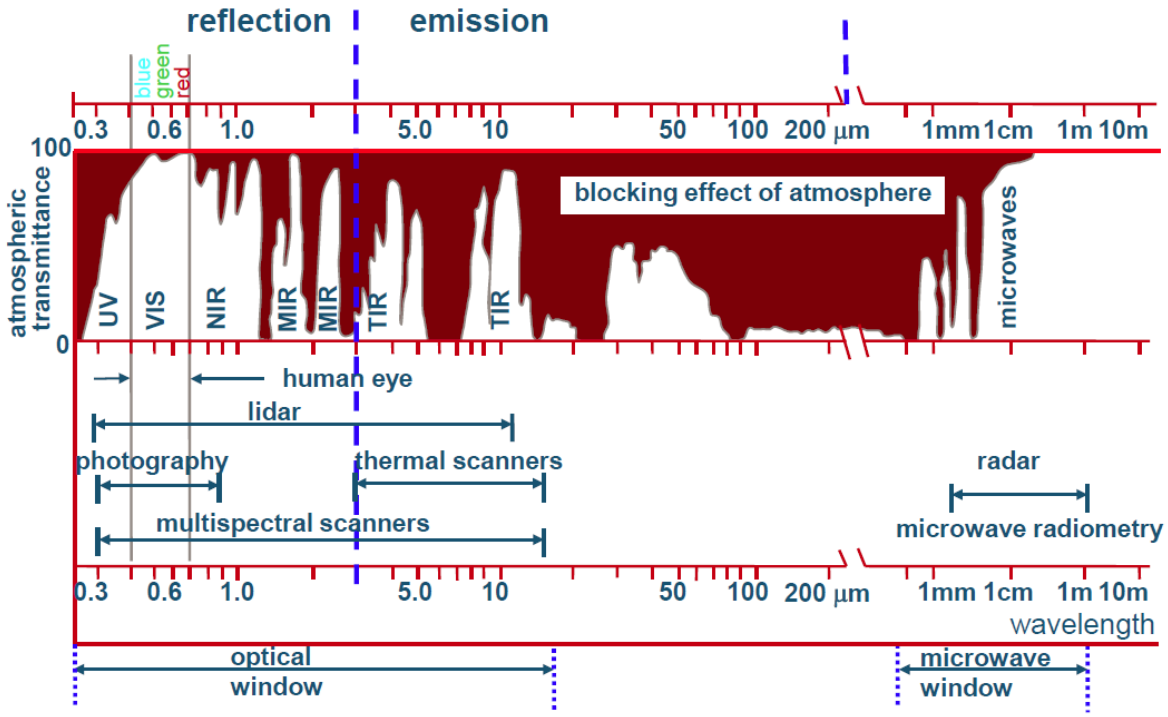

Figure 3.1.2. Atmospheric transmittance for EM radiation as a function of the wavelength (Clevers, Lecture - GRS-20306 - Remote Sensing: Optical Remote Sensing, 2017).

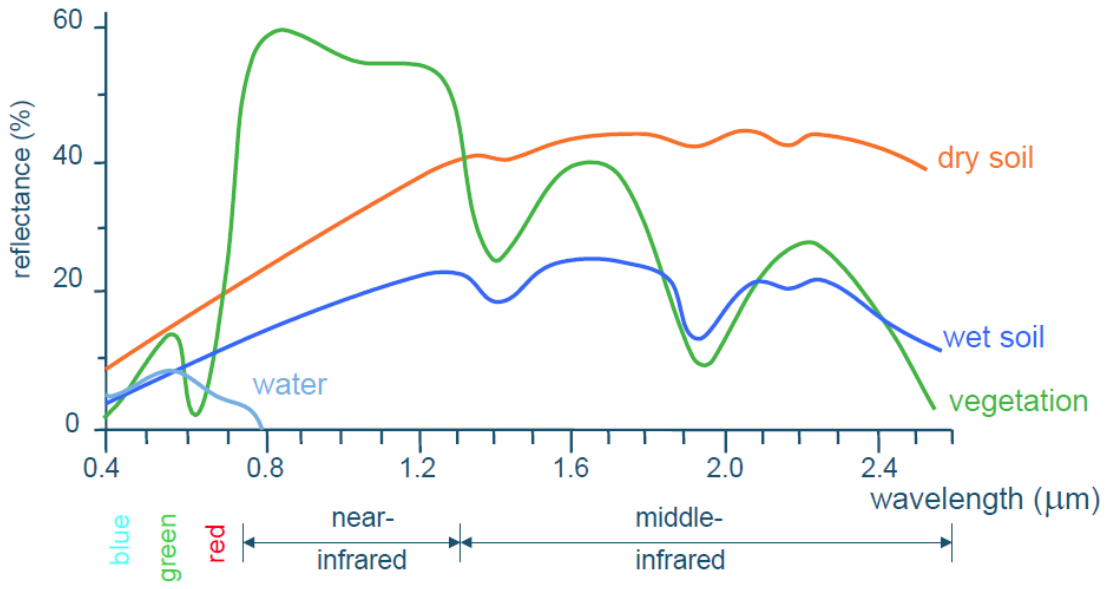

Figure 3.1.3. Spectral reflectance signatures for vegetation, soil and water (Clevers, Lecture - GRS-20306 - Remote Sensing: Vegetation indices - Statistical Methods, 2017).

3.2. Soil reflectance

Because bare soil reflectance is influenced by many factors, it is much more complicated to link one typical curve for the reflectance of soil (ITC, 2012). In contrast to vegetation, the amount of EM energy that transmits through soils is much lower. Therefore, spectral signatures of soil are related to the most superficial conditions (Chuvieco, 2016).

The main factors that determine the reflectance for bare soils are explained by Irons, Weismiller, & Petersen (1989). These are: texture and roughness; organic matter content; moisture content; and mineralogical composition.

Texture and roughness

These are the most important factors that affect the directional reflectance of bare soil and are independent of wavelength. Under laboratory conditions, smaller particles generally result in higher reflectance. However, clayey soils (final particle size distribution) are characterised by its lower overall reflectance than that of sandy soils (coarser particle size distribution). This is due the tendency of clay to aggregate and create surfaces with more height variations: a rough surface. This causes self-shadowing (darkening) effects and multiple scattering within the clayey soil, resulting in a decrease in reflectance. Surface roughness is expressed as the standard deviation of elevation points from the plane for a certain area (Lindenbergh, 2015). It is also referred to as the root mean square (RMS) roughness.

Organic matter

Organic matter largely influences the amount of reflection. An increase in organic matter causes a decrease in reflectance. When the organic content is above 2%, it will mask other absorption features in the EM spectrum.

Moisture content

Moisture generally results in an overall decrease in reflectance. This is explained by the internal reflections that occur in water that covers the soil surfaces and particles. Furthermore, the higher the moisture content of a soil, the more prominent the water absorption dips at 1.4 and 1.9 μm will be.

Mineralogical composition

Mineralogical composition affects the spectral curves of soil very specifically. This is related to the specific absorption dips of different minerals that are caused by *electronic processes* (active in the shorter wavelengths) and *vibrational processes* (active in the longer wavelengths). Iron-oxide content is a very important factor for the reflectance of soil. Iron causes electronic processes (charge-transfer of iron-ions) that is responsible for absorption features in the UV, VIS and NIR region of the EM spectrum. An increase in iron content will generally cause a decrease in reflectance.

Iron-ions are very common in soils due to their high solubility in water (Hunt, 1980). The resulting absorption features of iron on soil reflectance can be described by the following characteristics (Bartholomeus, Clevers, & Kooistra, 2015). Firstly, in the VIS region, a higher reflectance is produced in the green and red part than in the blue part. Secondly, in many parts of the spectrum, absorption of iron cause a decrease in reflection. Also, a higher iron content causes soil to appear darker and thus influences the colour of soil. Thirdly, iron causes many small absorption dips (and some larger dips) throughout the whole soil reflectance spectrum.

These influencing factors cause differences in soil reflectance curves, according to Stoner & Baumgardner (1981), given in Figure 3.2.1, where iron and organic matter are the largest influence.

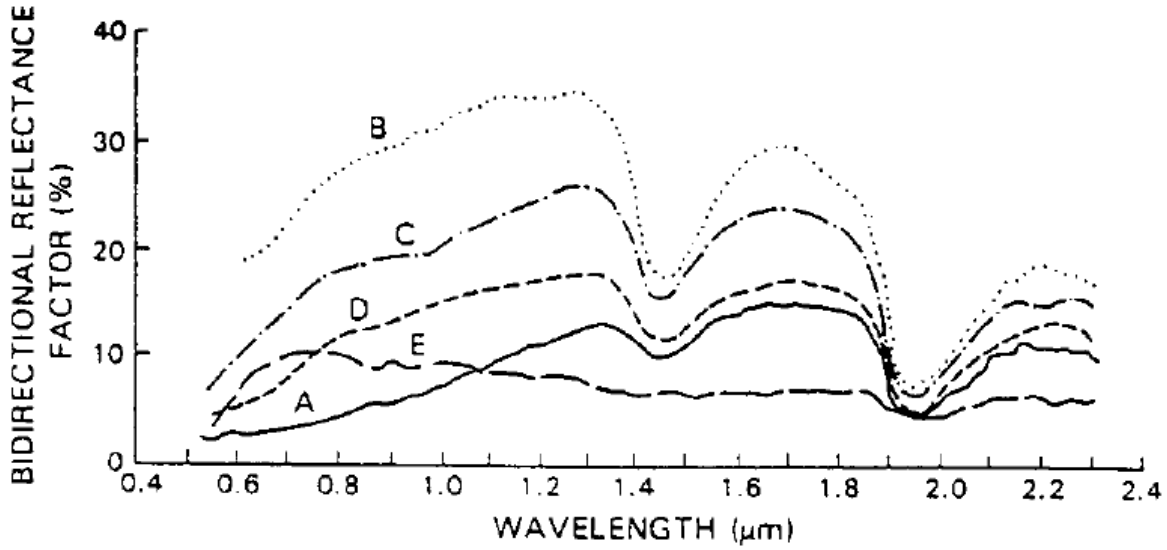

Figure 3.2.1. Spectral reflectance of five mineral soils (Stoner & Baumgardner, 1981):

A: soils having high (>2%) organic-matter content and fine texture.
B: soils having low (<2%) organic-matter content and low (<1%) iron-oxide content.
C: soils having low (<2%) organic-matter content and medium (1-4%) iron-oxide content.
D: soils having high (>2%) organic-matter content, low (<1%) iron-oxide content, and moderately coarse texture.
E: soils having high (>4%) iron-oxide content and fine texture.

3.3. LIDAR

There are three ways of sensing information about an object (Chuvieco, 2016). The first way of sensing information is the *reflection* of EM energy from an object. The Earth surface is illuminated by the sun and reflects a part of the EM energy: solar radiation is reflected. This occurs in the VIS, NIR and MIR part of the EM spectrum (Figure 3.1.2). A sensor, a satellite sensor for example, detects the energy and makes a recording of the signal. The recorded signal is then transmitted to a receiver. The second way of sensing information can be described by the *emission* of EM energy from an object on the Earth's surface. This occurs in the TIR (thermal infrared) part of the EM spectrum, particularly at about 10 μm. A sensor that is capable of detecting this energy is independent of light and can therefore be used for observations during day and night. The third way of sensing information is based on the combination of both reflected and emitted energy from an object. In this case, an active sensor, which in contrast to a passive sensor, has its own source of energy. It has the ability to send pulses to the target objects and record the reflected energy from the objects after which a characterization can be made about the object. An overview of sensors in different domains is illustrated in Figure 3.3.1. LIDAR is an active sensor. It has a built-in source of radiation.

LIDAR stands for light detection and ranging (or laser imaging detection and ranging). It has many applications in different fields and sectors such as remote sensing, geology and seismology. It is an active remote sensing technique that works with polarized light in the optical domain: typically in the UV, VIS or NIR range. Light pulses with a finite and constant velocity are transmitted by the source, the laser scanner (Vosselman & Maas, 2010). The laser emits the pulses in a very narrow beam of monochromatic light (one wavelength or colour). Lasers specifically emit radiations of high intensity (ITC, 2012). When the pulses are reflected by the targets back to the source, the distance or the range from the source to the object can be determined:

$$\rho = \frac{c}{n}\frac{\tau}{2} \qquad (3.2)$$

Where:

- ρ is the range between the source and the object or target (in m)
- c is the velocity of light in a vacuum (299 792 458 m s^{-1})
- n is the correction factor for air (in Hz or s^{-1})

- τ is the round trip, the time-of-flight of light travelling from the source to the target and back to the source (in s)

When the exact position and orientation of the sensor is known, the X, Y and Z coordinates of the reflected object can be determined. The collected data is described as a 3D point cloud with X, Y and Z coordinates of every point. Some laser-based instruments also measure the amount of the reflected energy from an object. This is referred to as the *intensity* and can be used to produce intensity images (ITC, 2012). As mentioned before, the amount of reflected energy or intensity is affected by many factors such as surface roughness, texture, mineralogical composition, organic matter and moisture content. Furthermore, there are laser-based instruments that can store *RGB*-values in the point cloud data and produce an RGB-image, by using a red, green and blue filter array in front of the detector.

Laser scanners can be divided into two groups: kinetic laser scanners (example: airborne) and static laser scanners. Terrestrial laser scanners (TLS) are static, they have a fixed position, where the laser is mounted on a tripod (Vosselman & Maas, 2010). The laser scanner used for this project is a terrestrial laser scanner: the Leica Scan Station C10.

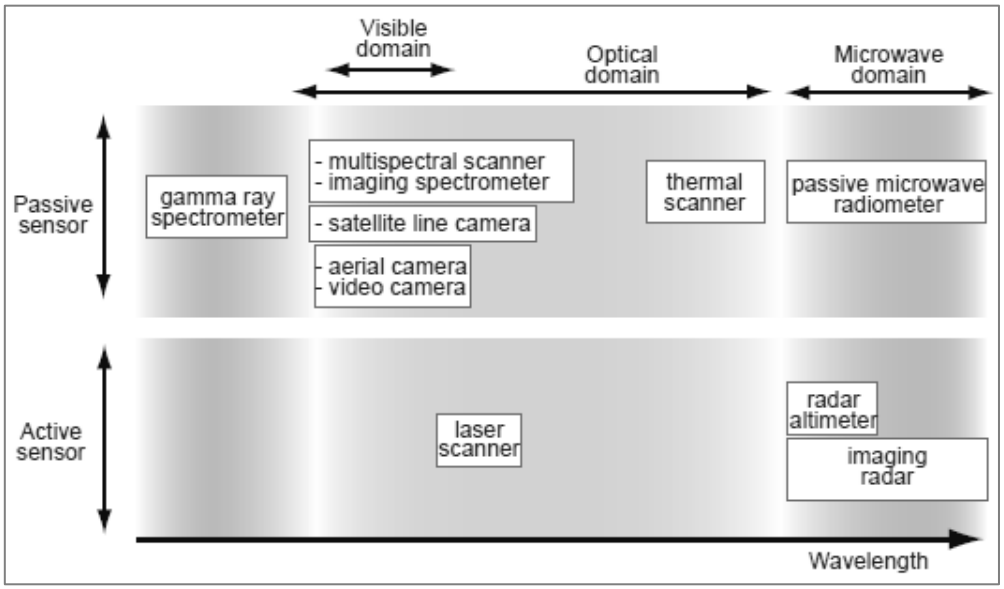

Figure 3.3.1. Active and passive sensors acting in different domains of the EM spectrum (ITC, 2012).

3.4. Leica C10 laser scanner

The Leica C10 laser scanner is active in the green part of the VIS region, at a wavelength of 532 nm. Technical specifications of the laser scanner can be found in Table 3.1.

For this research, the highest resolution (highest amount of points per area) was chosen as the objects to be scanned are very small. The collected data is a 3D point cloud with X, Y and Z coordinates of every point, as mentioned before. To each point, an R-, G-, B-value (of the image) is assigned as well as the intensity value I. So the point cloud is stored as a long list of X-, Y-, Z-, I-, R-, G- and B-values. This data set can be exported from the laser scanner and opened in Cyclone, which is the program that comes with the Leica C10 laser scanner.

Before scanning the samples, an exercise on a core sample (Figure 3.4.1) of the Geo-Engineering department was performed in order to get acquainted with the laser scanner. The set-up before scanning the core samples is visualized in Figure 3.4.2. The samples were stored in the climate room of the Geo-Engineering basement, to prevent the samples from drying out. The samples were lain horizontally on the floor and the laser was positioned some distance straight in front of the samples.

Table 3.1. Specifications of Leica Scan Station C10 (Leica Geosystems AG) .

Property	***Value***
Wavelength	532 nm (green, VIS)
Minimum range	0.1 m
Maximum range	300 m
Scan rate	Up to 50,000 points/sec
Field of view, vertical	270°
Field of view, horizontal	360°
Accuracy, position	6 nm
Accuracy, distance	4 nm

Figure 3.4.1. Practicing with the Leica C10 laser scanner.

Figure 3.4.2. Set-up before scanning the core samples.

4. METHODOLOGY

After laser scanning, classification of a core sample can be assessed using the features (information) from the raw 3D point cloud of the sample. The features used for the classification of each sample are RGB values (a colour image), intensity values (the amount of reflected energy), surface roughness and height differences. As mentioned in Section 3.2, factors that will most likely have a large influence on the intensity signal are particle size distribution and surface height variation (roughness) (Chuvieco, 2016).

In this section, the method chosen for the classification of a core sample is explained in detail. The proposed workflow is as follows:

Raw point cloud → Segmentation → Least squares fitting → Discretization → Rasterization → Stacking → Digital Image Classification → Assignment of classes

4.1. Segmentation

Laser scanning usually generates a point cloud consisting of millions of points, while the area of interest is only the sample itself, that is, without the area surrounding it. Therefore, the first thing that has to be done is to select the points that represent the sample and use this segment for further processing.

4.2. Least squares fitting

In order to get information about the surface roughness of a sample, a plane has to be fit through the points. One popular approach for plane fitting is least squares fitting (LSF) (Lindenbergh, 2015). LSF is an iterative algorithm where the best-fit plane is approximated by finding the perpendicular distance (least squares distance) from the measured point to the fitted plane. In a point cloud data set of a sample, each point consists of an X, Y and Z coordinate. LSF is applied to each Z coordinate, the measured height of the point, to calculate its perpendicular distance to the fitted plane. The equation for a plane of the measured height can be expressed as:

$$z(i) = a \cdot x(i) + b \cdot y(i) + c \tag{4.1}$$

Where:

- $z(i)$ is the Z coordinate of the ith point (the measured height)
- a and b are normals of the plane
- $x(i)$ and y(i) are the X and Y coordinates of the ith point
- c is a residual between the observations (z) and the model

When written in vector notation, Equation 4.1 can be rewritten as:

$$\begin{bmatrix} x_1 & y_1 & 1 \\ x_2 & y_3 & 1 \\ \vdots & \vdots & \vdots \\ x_i & y_i & 1 \end{bmatrix} \begin{bmatrix} a \\ b \\ c \end{bmatrix} = \begin{bmatrix} z_1 \\ z_2 \\ \vdots \\ z_i \end{bmatrix} \tag{4.2}$$

Or:

$$A\boldsymbol{x} = \boldsymbol{b} \tag{4.3}$$

Where:

- A is the model matrix
- $\boldsymbol{x}$ is the vector of parameters (unknown)
- $\boldsymbol{b}$ is the vector of observations: the measured height values

The goal is to find a vector $\hat{\boldsymbol{x}}$ such that the distance from $A\boldsymbol{x}$ to $\boldsymbol{b}$ is minimized (Figure 4.2.1).

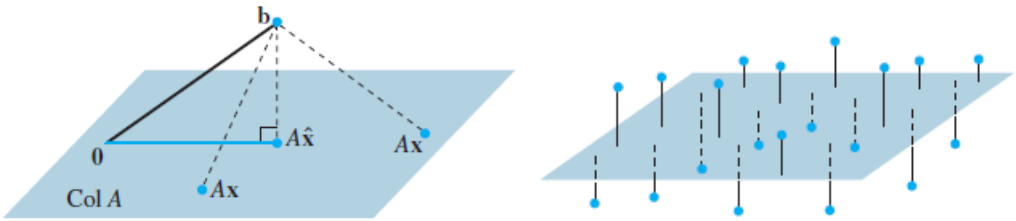

Figure 4.2.1. Left: Vector $\boldsymbol{b}$ is closer to $A\hat{\boldsymbol{x}}$ than to $A\boldsymbol{x}$ for other $\boldsymbol{x}$. Right: Least-squares-plane of multiple points. After Lay (2012).

When A is an m x n matrix and the following statements are true (Lay, 2012):

- Equation $A\boldsymbol{x} = \boldsymbol{b}$ has a unique least-squares solution for each $\boldsymbol{b}$ in the model space
- The columns of A are linearly independent
- The matrix A^TA is invertible

Then, the least-squares solution $\hat{\boldsymbol{x}}$ is given by:

$$\hat{\boldsymbol{x}} = (A^TA)^{-1}A^T\boldsymbol{b} \tag{4.4}$$

The minimal distance between the observations $\boldsymbol{b}$ and adjusted observations $\hat{\boldsymbol{b}}$ (orthogonal projection of $\boldsymbol{b}$) is defined by the error vector $\hat{\boldsymbol{e}}$:

$$\hat{\boldsymbol{e}} = \boldsymbol{b} - \hat{\boldsymbol{b}} \tag{4.5}$$

$$\hat{\boldsymbol{e}} = \boldsymbol{b} - A \cdot \hat{\boldsymbol{x}} \tag{4.6}$$

Vector $\hat{\boldsymbol{e}}$ is the perpendicular distance from the measured height of a point to the fitted plane.

Each point in a point cloud of a core sample now has the following features with indicated dimensions:

- X-, Y- and Z-value (m) XYZ-coordinates where Z is the measured height (b)
- R-, G- and B-value (-) RGB-values ranging from 0-255 (digital number)
- I-value (-) a measure of intensity ranging from 0-1
- Z_{plane}-value (m) $\hat{b}$: the height of the fitted plane
- dZ-value (m) $\hat{e}$: the perpendicular distance from Z to Z_{plane}

4.3. Discretization and stacking

Not all features mentioned in Section 4.2 are used for the classification. As explained earlier, the features used for the classification of a sample are the RGB values (R, G, B), intensity values (I), height differences (dZ) and surface roughness (σ_z).

Surface roughness or RMS roughness is calculated using the following equation, with n as the amount of points for a certain area (Lindenbergh, 2015).

$$\sigma_z = \sqrt{\frac{\hat{e}^T\hat{e}}{n}} \tag{4.7}$$

For the classification, a multiband raster is used and therefore six 2D-grids or rasters containing the following features are made: R, G, B, I, dZ and σ_z.

These rasters have columns corresponding to the user-defined number of steps in the Y-direction, starting from the minimum value of Y and ending with the maximum value of Y, and rows corresponding to the former mentioned step size, starting from the minimum value of X and ending with the maximum value of X. In order to create these rasters, discretization in X- and Y-direction is performed (Figure 4.3.1). During this process, for each of the rasters, the mean value of all points per cell is calculated. For the surface-roughness raster, equation 4.7 is calculated for each cell where n represents the amount of points occurring in a cell and $\hat{e}$ is the mean of the perpendicular distances of the Z-values to

the plane of that cell. Finally, the rasters are stacked to create a multiple-band raster on which digital image classification is performed.

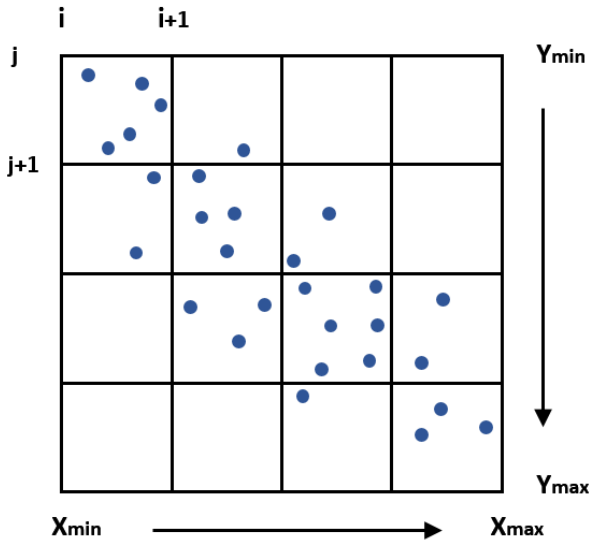

Figure 4.3.1. Schematic 2D visualisation of discretization in X- and Y-direction for randomly distributed points representing a point cloud of a core sample. Each feature raster will have the same spatial structure: same amount of rows, columns and user-defined cell size.

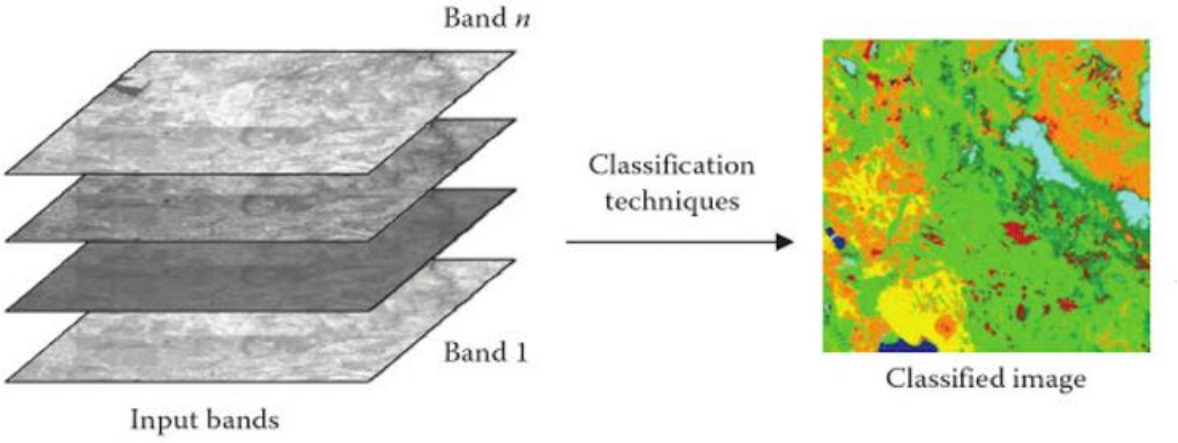

Figure 4.3.2. A multiband-raster (stacked) is used for classification (Chuvieco, 2016).

4.4. Digital image classification

The goal of this research is to obtain a digital image classification of a sample that represents the ground truth data. The result is a thematic map where pixels are grouped, or “clustered”, based on common characteristics. Every pixel represents one category (class), in the case a soil type. Usually, the classification of soil is carried out visually. However, the main advantage of digital image classification is that it is a more robust and spatially consistent method, especially when studying large areas (Chuvieco, 2016).

The input image is a multiband-image, the stacked rasters explained in Section 4.3, where each pixel of each raster contains a quantitative value. When classification is applied to the input image, the output image results in a thematic map that has the same spatial structure as the former. The only difference is that the pixel values have been converted from quantitative data to qualitative (nominal) data, where every pixel contains a number that now represents a category. Therefore, despite of its numeric values, the output data is considered as a nominal measurement scale.

Digital image classification is carried out in three main steps (Chuvieco, 2016):

1. Training phase
2. Assignment phase
3. Assessment of results

The objective of the training phase is characterizing categories (the soil type) that are distinguishable from each other. Characterization is based on the pixels that are representative for a certain study area (the core sample). It is desirable to achieve a result that is as accurate as possible, hence, with a pixel size (or grid size) that is as small as possible. Two types of classification methods can be distinguished: supervised and unsupervised. In the case of supervised classification, clusters are defined by the user, based on previous knowledge of the area (training data), to derive the statistics of each class. These clusters represent the classes. In contrast, unsupervised classification uses a clustering algorithm that finds the number of clusters automatically. The user needs to assign classes to the clusters afterwards. No prior knowledge of the area is required.

The classification method chosen for this research is unsupervised classification. Commonly used clustering algorithms are Principle Component Analysis (PCA), K-means and ISODATA (Lindenbergh, 2015). Since ISODATA is used for this research, only ISODATA will be discussed.

The ISODATA (Iterative Self-Organised Data Analysis Technique) algorithm (Duda & Hart, 1973) is known for its flexible and robust scheme. It is an iterative process that can be described in five steps:

1. Random means for each cluster (cluster centres) are assigned by the software. The number of clusters is defined by the user.
2. The software assigns each pixel to the mean that is the nearest, the minimum Euclidean distance.
3. After performing the first iteration, new means of each cluster are recalculated, based on its pixel members.
4. Second iteration: pixels are re-assigned to the nearest cluster centre.
5. Step 3 and step 4 are repeated until no more pixels, above a user-defined threshold, migrate to another cluster.

Before executing unsupervised classification on a multiband-raster of a core sample, a set of parameters should be defined. The parameters chosen for this research are the minimum cluster size (cell size), the maximum number of clusters (cells) and the sampling interval (size of the block of cells used for the cluster calculation).

After performing the classification using the defined parameters, the user analyses the classified image of the core sample and compares it with the ground truth data. The user subsequently has the option to improve results by changing the parameters and performing the unsupervised classification repeatedly until the desired result is achieved.

4.5. Software

Software applications used for processing the point cloud data for this research were Cyclone, CloudCompare, Matlab and ArcMap. These are explained briefly in this section.

4.5.1. Cyclone

Cyclone is the software application that comes with the Leica C10 laser scanner. It is used to register and geo-reference the scanned data to a common coordinate system. Subsequently, the data was converted to a format (.PTX) that is compatible with other applications, such as CloudCompare, for further data processing.

4.5.2. CloudCompare

After extracting the data from Cyclone, the data is imported into CloudCompare. CloudCompare is an application that processes 3D point cloud data. For this research, it was used for selecting the point clouds of each core sample as discussed in Section 4.1. Each of the selected segments (core samples) were saved as a text file (.ASCII) and a point cloud library file (.PCD).

4.5.3. Matlab

Matlab is a programming application used for all kinds of mathematical applications. After the use of CloudCompare, Matlab was used to read the text file and point cloud library file of each sample. Least squares fitting and discretization, as explained in Section 4.2 and 4.3, were performed in Matlab. Matlab codes can be found in Appendix E.

4.5.4. ArcMap

ArcMap is the primary application of ESRI's ArcGIS and is used to represent geographic information in multiple layers (ESRI, 2017). For this research, it was used to stack the rasters, that were created in Matlab, to a multible-band image. Next, unsupervised classification was performed on the multible-band image using the Iso Cluster Unsupervised Classification Tool. Finally, ArcMap was used for a final representation of the classified images. The ArcMap models can be found in Appendix G.

5. RESULTS & DISCUSSION

Iso cluster unsupervised classification could only be executed for three of the five core samples, namely: L9, L12 and L14. However, the final result for sample L9 appeared to be the most representative when compared to ground truth data. The used cell size for all samples was 0.0030 m, as it provided the best classification result.

Section 5.1 discusses the results for sample L9 in detail, starting with the intermediate results: the feature rasters. Subsequently, the final result after performing the classification is shown and discussed. As a reference, a photo of the original sample is illustrated next to each classified image. Section 5.2 and Section 5.3 will shortly discuss the final result for sample L12 and L14 respectively. Section 5.4 covers the classification of sample L15 and L19.

5.1. Sample L9

5.1.1. Intermediate results

The intermediate results are the feature rasters (R, G, B, dZ, I and σ_z) as obtained from Matlab, given in Figure 5.1.1. For easier interpretation, these results are displayed as shown in Figure 5.1.2. Interpretations are based on the descriptions of the core sample and knowledge of soil reflectance. The detailed description of the core sample, as performed by Fugro, can be found in Appendix 0. Soil reflectance was covered in Section 3.2.

Layer A (0 - 20 cm)

From visual inspection, the load cast structure, indicated by the star in Figure 5.1.2, is characterized as a clay. It represents an intrusion into layer A. Layer A is described as a sand containing 10-20% glauconite (Table 2.1). At first sight, it seems unexpected that the load cast structure shows higher values for intensity than layer A. As explained in Section 3.2, soils having a higher moisture content will absorb more EM energy, and thus will reflect less EM energy than dryer soils. Generally, clayey soils hold more water than sands and thus will produce lower intensity signals. Furthermore, from Figure 5.1.2, one should remark that the roughness values for the load cast structure are higher than those for layer A. This may be explained by the aggregation of clay particles forming a rough surface, as explained in Section 3.2. Therefore, regarding the moisture content and surface roughness of the load cast structure, one may expect lower intensity values for the load cast structure than for layer A. However, layer A contains 10-20% glauconite which is an iron-bearing mineral. Section 3.2 explained that iron-bearing minerals largely contribute to a decrease in reflectance of bare soil. This may be an explanation for layer A (a sand) having lower intensity values than those of the load cast structure (a clay).

Layer B (20 - 38 cm)

From Table 2.1, layer B represents a clay. It shows a higher overall intensity than layer A and roughly the same overall intensity as the load cast structure (Figure 5.1.2), which is not surprising as they represent the same type of soil. However, layer B shows lower values for the surface roughness than the load cast structure in layer A. This difference may be explained by the load cast structure that most likely resulted from the drilling, and subsequently caused the clay particles to aggregate, resulting in an increased surface roughness.

Another striking feature should be noticed from the intensity image in Figure 5.1.2. At a depth of 30 cm, a small area showing a decrease in intensity value is visible (dark spot). From the core sample descriptions (Figure B.2, Appendix 0), this area represents an inclusion of sand having a glauconite content of 30-50%. This explains the decreased values of intensity of that area.

Layer C (38 – 54 cm)

Layer C represents a very sandy loam containing 5% glauconite (Table 2.1). According to Figure 5.1.2, layer C shows much higher intensity values than those of layer A. This may be explained by the glauconite content in layer A (a sand) which is about three times higher than that of layer C, contributing to the increased overall intensity in layer C.

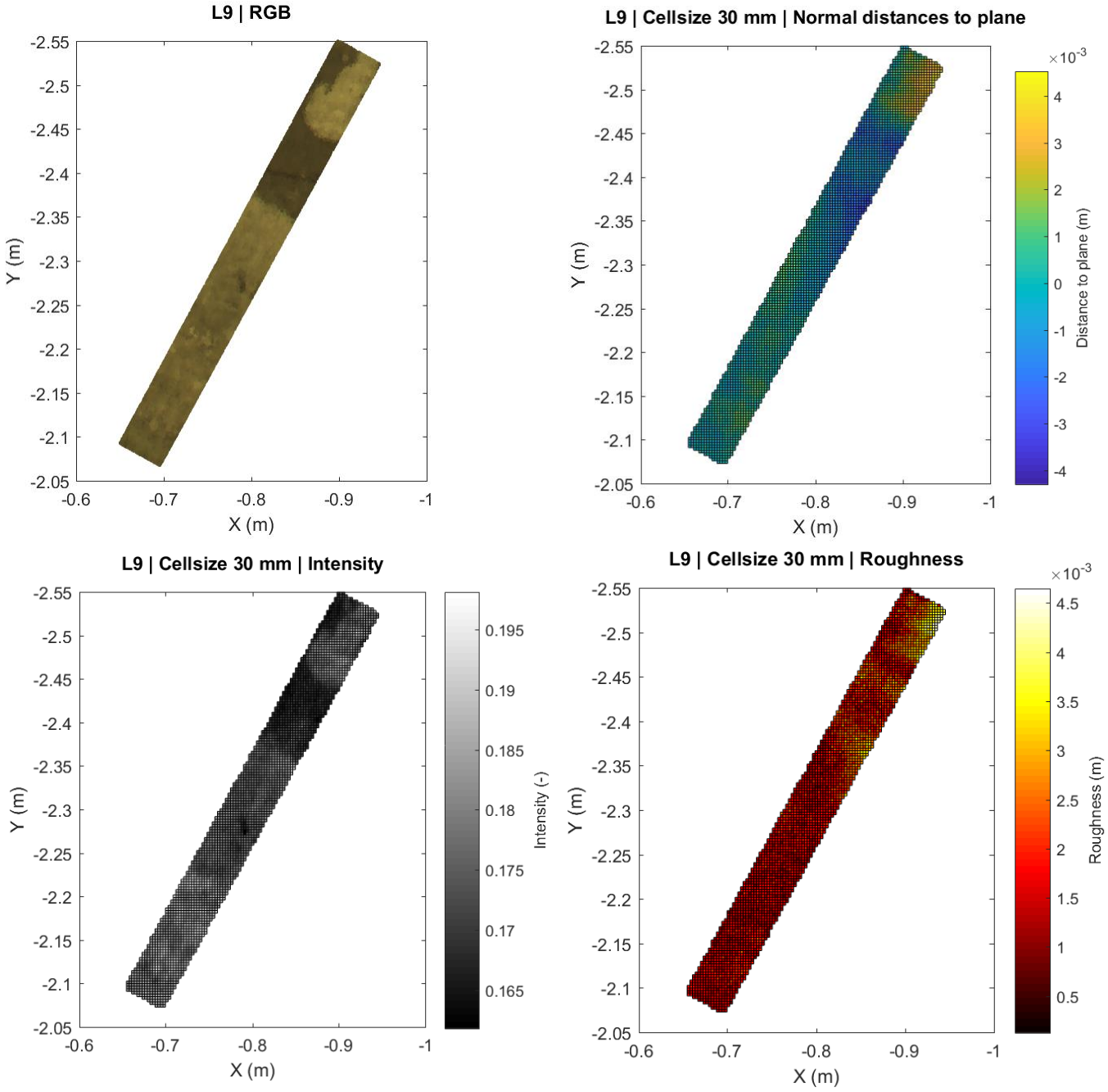

Figure 5.1.1. Intermediate results of sample L9: features (R, G, B, dZ, I and σ_z) used for performing iso cluster unsupervised classification.

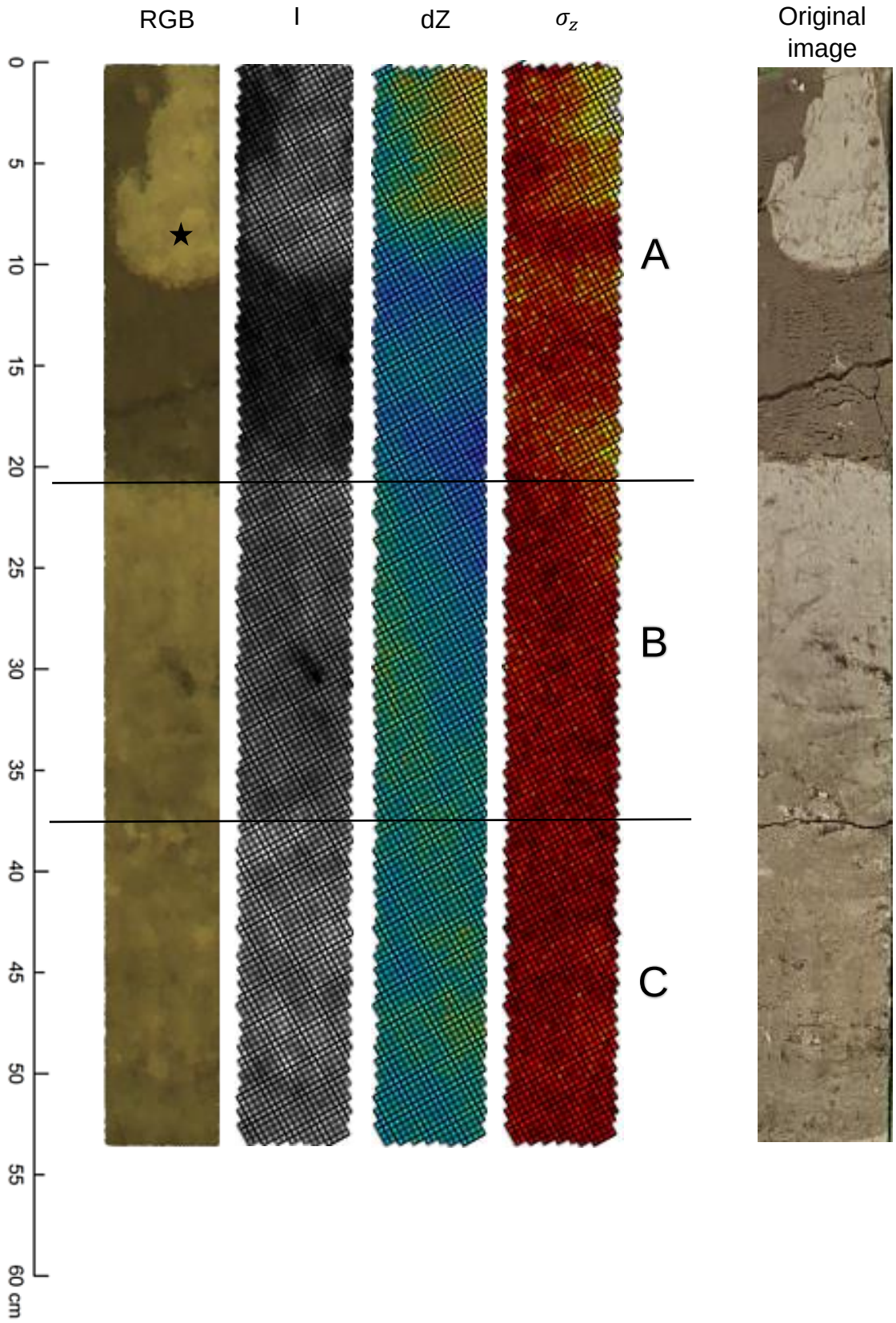

Figure 5.1.2. Intermediate results of sample L9 with indicated boundaries between the layers A, B and C (I = intensity, dZ = normals-to-plane, σ_z = roughness).

5.1.2. Final result

The result after performing iso cluster unsupervised classification is shown in Figure 5.1.3. Three clusters (labelled “1”, “2”, and “3”) are created representing three categories of soil type. Two classified images are displayed next to each other. When observing the right image, one may notice the smoothened edges of the pixels. Bilinear interpolation has been applied to the left image, which is a first-order interpolation between four adjacent input pixels, a weighted average.

Layer A (0 - 20 cm)

Layer A shows large similarities when compared to the original image (Figure 5.1.3). The boundary between layer A and layer B, indicated by feature (c), corresponds to the boundary in the original image. Also, one may notice that feature (a) in the classified image corresponds to the load cast structure in the original image, which represents a clay. The same can be said about feature (b), labelled as cluster 1, which in the original image represents a sand, as explained in the previous section.

Layer B (20 - 27 cm) and layer C (27 - 54 cm)

A feature that is clearly visible on both classified and original image, is the inclusion of sand containing the higher glauconite content, as mentioned in the previous section. This inclusion is indicated by feature (d) in Figure 5.1.3.

The boundary between layer B and layer C has moved 10 cm upwards compared to the same boundary in Figure 5.1.2 from the previous section and the ground truth data (Appendix 0). No clear explanation can be found for this appearance. Even, after performing the unsupervised classification several times by using different combinations of bands, no changes occurred in the final result. These results can be found in Appendix D. From these results, the following conclusions could be made:

- Unsupervised classification using the bands (R, G, B), resulted in two clusters. Thus classification based only on an RGB-image does not provide the desired result.
- Unsupervised classification using the bands (R, G, B, DZ); (R, G, B, I); (R, G, B, RO), where DZ is the normals-to-plane band and RO is the roughness band, showed minor differences between the results. Therefore, it may be assumed that the influences of the normals-to-plane, intensity values and surface roughness values are equal. This may be explained by the strong correlation between these three features.

The last step in digital image classification is assigning labels to the cluster, as mentioned earlier. Considering all findings mentioned above and based on the ground truth data, the clusters are classified as follows:

- Cluster 1 – Sand
- Cluster 2 – Loam
- Cluster 3 – Clay

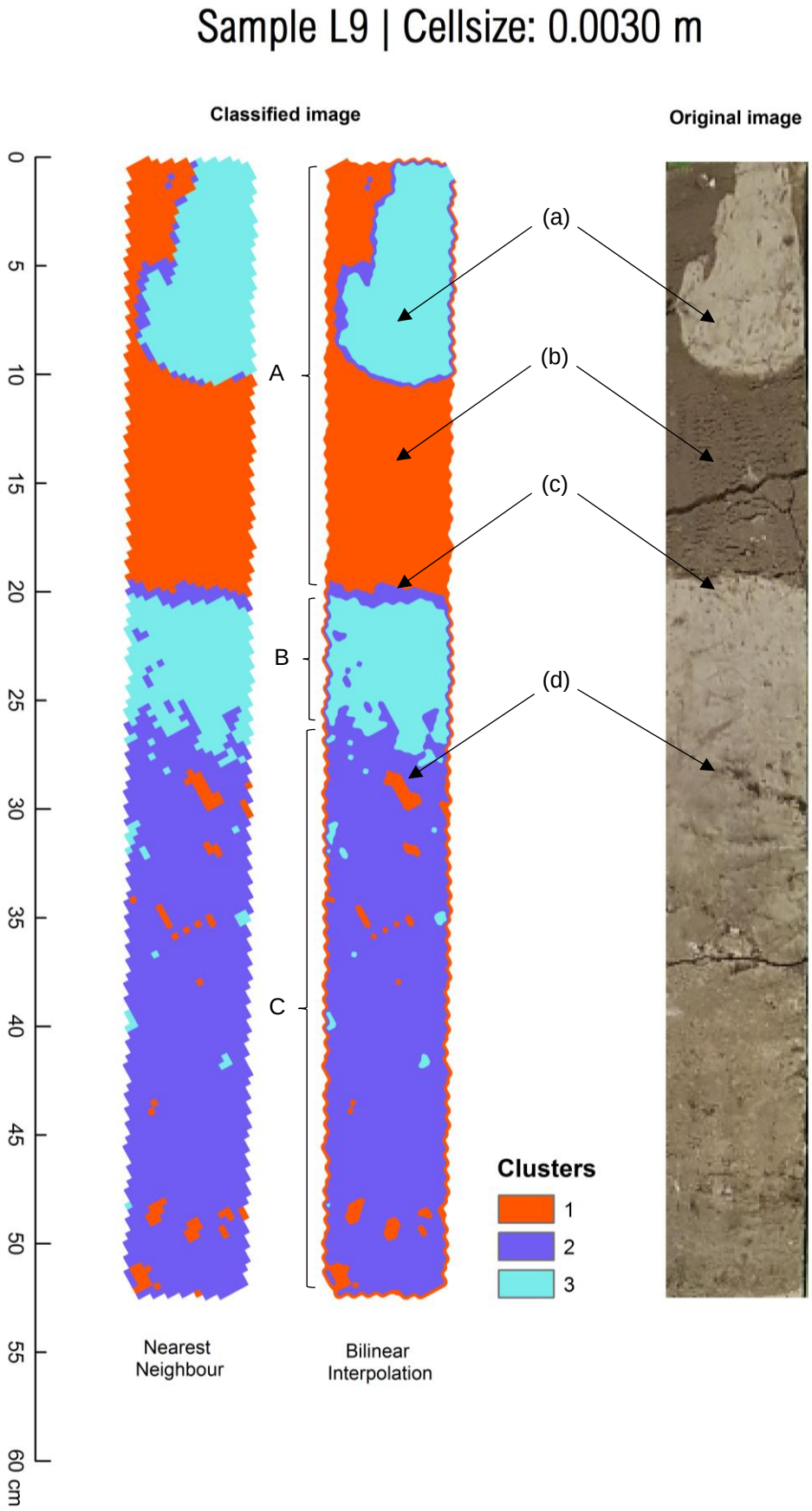

Figure 5.1.3. Final result of sample L9 after performing iso cluster unsupervised classification.

5.2. Sample L12

The final result of sample L12 is given in Figure 5.4.1. The following features were found by comparing the classified and the original image:

- Feature (a) and feature (c) both represent Cluster 4, assuming these clusters to be of the same soil type. When compared to original image and the ground truth data of sample L12 (Figure B.3, Appendix 0), these features are characterized by sand.
- Feature (b) in the classified image, although slightly visible, may be recognized as the laminations that are visible in the original image on the right.

Classification of sample L12 does not result in the desired categories that are present in the ground truth data (original image). An explanation for this may be the minimal differences between the layers in the actual core sample for the laser scanner to discriminate between the spectral reflectance signatures from the core sample.

5.3. Sample L14

Figure 5.4.2 shows the final result of sample L14. The ground truth data shows that four layers can be recognized. From top to bottom: sand, sand, clay, sand (Table 2.1 and Figure B.4, Appendix 0). When comparing the classified result in Figure 5.4.2 with the original image, the following conclusions could be made:

- The only layer clearly visible in the classified image is the upper layer, indicated as Cluster 1, representing a sand when comparing it with the ground truth data.
- Feature (a) represents a minor fault and feature (b) represents a boundary between sand and clay.

Again, the classification of sample L14 is not representative for the actual data. This may be caused by the same reason as mentioned for sample L12 (previous section).

5.4. Sample L15 & L19

Unfortunately, iso cluster unsupervised classification could not be performed on sample L15 and L19, even after trying out different cell sizes. By visual inspection (Table 2.1 and Figure B.7) it was concluded that both samples consisted out of one layer, which might be a reason why classification could not be executed on these samples as differences within the core samples were not large enough to show distinguishable soil reflectance spectra.

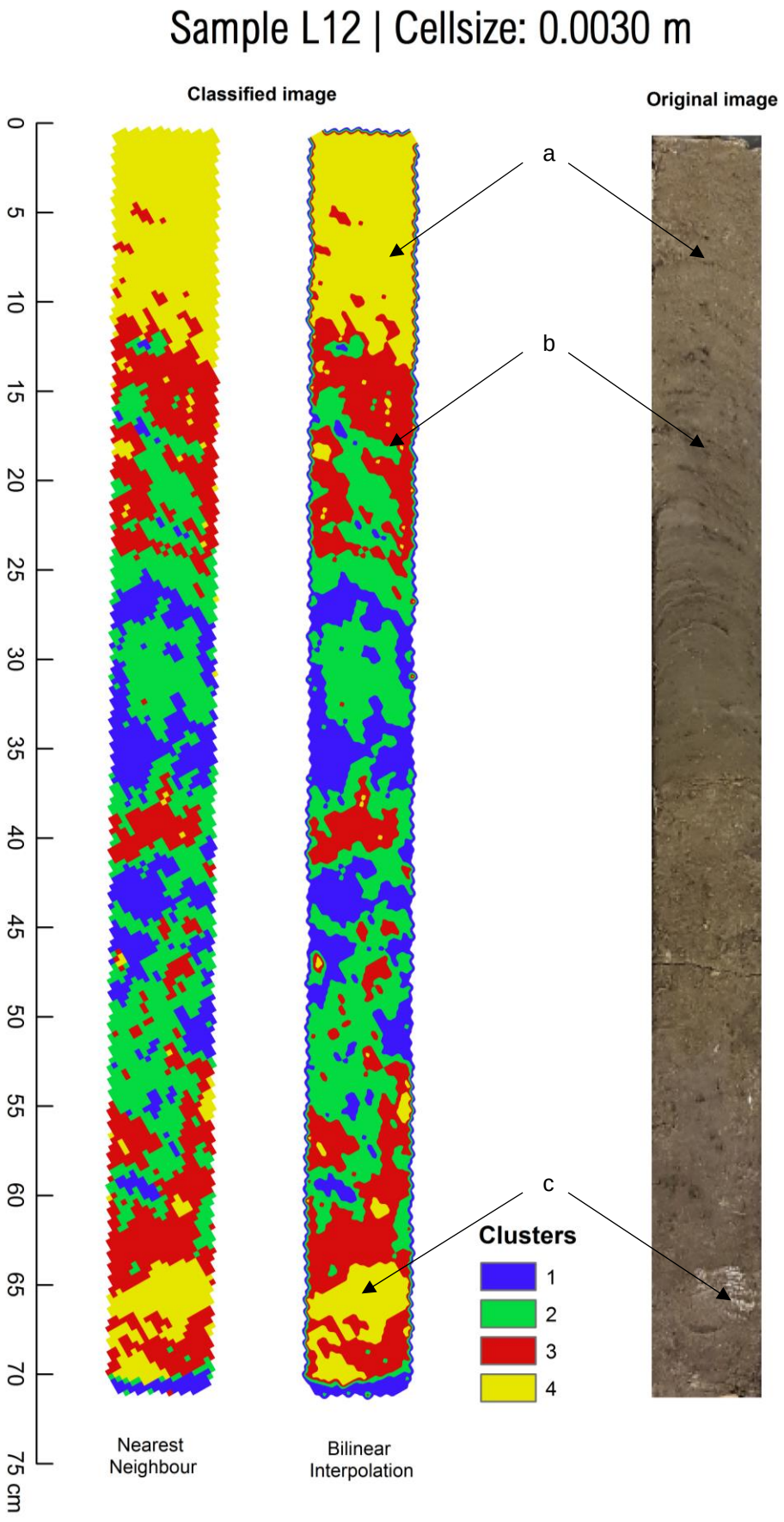

Figure 5.4.1. Result of sample L12 after performing iso cluster unsupervised classification.

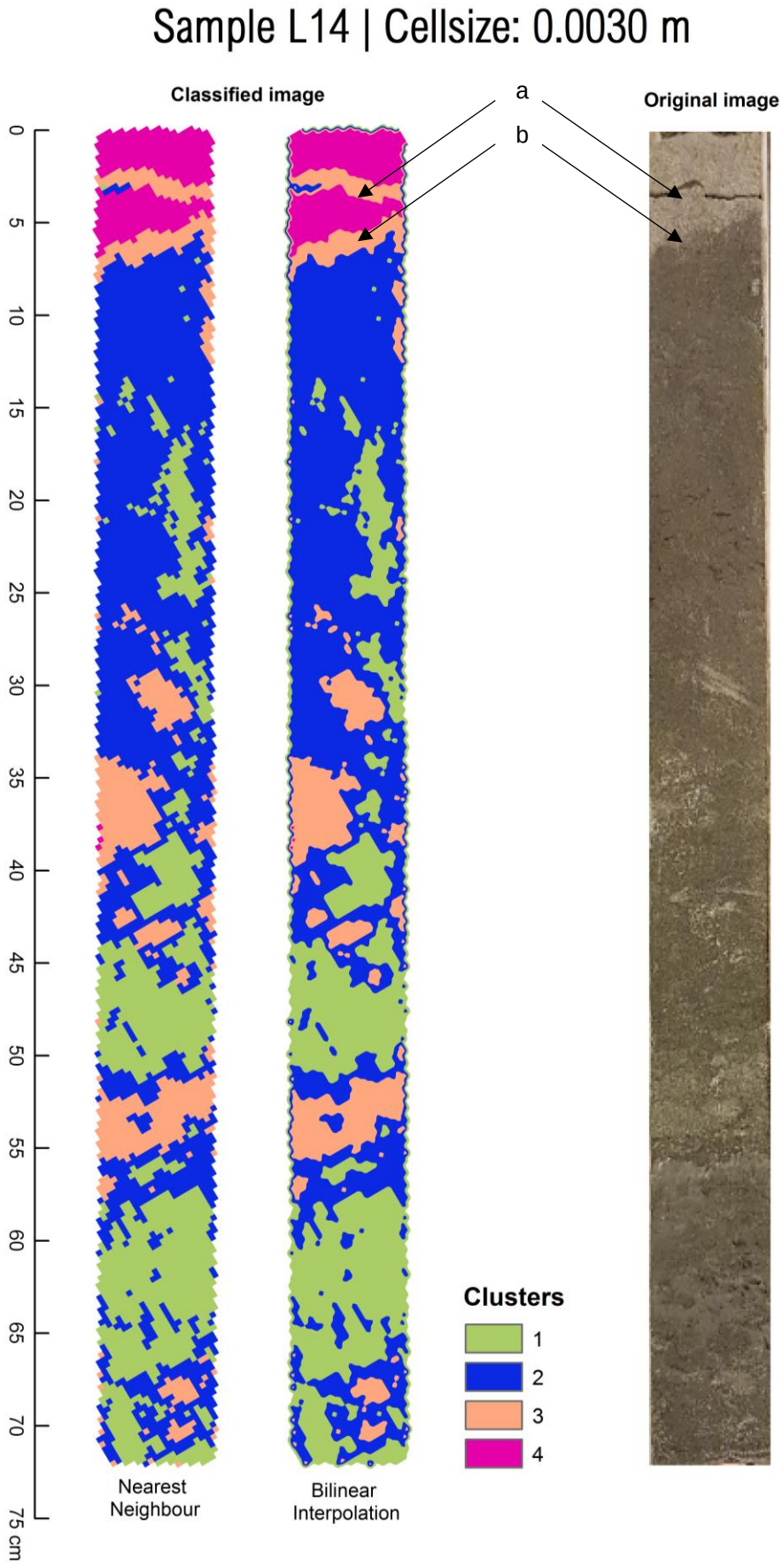

Figure 5.4.2. Result of sample L14 after performing iso cluster unsupervised classification.

6. CONCLUSION

The research question in this thesis states whether terrestrial laser scanning can be used as an automated method to improve core sample classification. To provide an answer to the research question, the following sub-questions were defined:

- *What are the advantages of this method compared to the current (in-situ and laboratory) methods?*
  The main advantages of digital image classification are that its method is more robust and spatially consistent. Although data acquisition may be fast, processing may be time consuming dependent on the capacity of computers.

- *Can classification using TLS be performed on all core samples and how reliable are the results?*
  Digital image classification provided results for three of the five samples, however, only one showed good results: sample L9. The classified images of sample L12 and L14 were less promising after comparing them with ground truth data, although some features could be identified. Classification could not be performed on sample L15 and L19, a possible explanation could be that the variability within both samples was not large enough to discriminate between different reflectance spectra.

- *For what core samples can this method be used and for what applications is it not suitable?*
  This method could be used for core samples that show sufficient variability within for the laser scanner to discriminate between the reflectance spectra of the sample. This was demonstrated for sample L9. If a sample shows too little variability, it is difficult to distinguish soil spectral signatures. This would infer that for these homogeneous core samples, this method is not suitable, as was demonstrated for sample L12 and sample L14.

- *What factors influence the classification result of a core sample and how? What factor is the largest contributor and why?*
  In general, the main factors that influence the reflected signal from TLS are texture and roughness, organic matter, moisture content and mineralogical composition. For this research, the main factors that influenced the final results of the samples were the glauconite content and surface roughness. Both factors generally cause a decrease in reflectance. Glauconite is considered to be the largest contributor to decreasing the intensity signal and thus the classification result, explained by the charge-transfer of iron-ions that cause absorption in the UV-VIS-NIR range. However, LIDAR emits pulses in a very narrow beam of monochromatic light (one colour). Thus, when studying the reflectance spectrum, a consequence may be the omission of characteristic features for a certain soil type which will influence the classification of a soil.

Can terrestrial laser scanning be used as an automated method to improve core sample classification?

Considering all answers stated above, one can conclude that terrestrial laser scanning alone would most often cause erroneous results when classifying soil.

7. RECOMMENDATIONS

A more efficient discretization method

When discussing the workload required to process the point cloud data, a more efficient discretization method could be chosen. In the case of the current discretization method, for *each* cell, Matlab has to run through *all* points in *both* X- and Y-direction to find matching values for each cell. Although, the running time was not an issue regarding the small data sets of the samples, it could be very time consuming for larger data sets. A solution could be to rotate the sample, so the raster only consists of cells that have values, thus NoData cells are removed. Next, all data points could be sorted in both X- and Y-direction, so that Matlab only needs to run through each cell one by one.

Supervised classification

The classification method chosen for this research was unsupervised classification. However, supervised classification may be more accurate but strongly depends on the training data. Gathering qualitative training data requires more time and could result in higher cost. The method is also criticized for being biased and superficial (Chuvieco, 2016). But when used for smaller data sets, such as the core samples for this research, supervised classification may provide more accurate results given that the training data is easy to acquire and costs will be limited due to the small size of the data sets.

Broadening the wavelength range

Most importantly, the laser scanner used for this research, the Leica C10 laser scanner, emits pulses in a very narrow beam of monochromatic light, at a wavelength of 532 nm (green part of the visible range). Using additional bands in other parts of the EM spectrum, such as the NIR range, could reveal new features that were not visible in the VIS range. The combination with another scanner (e.g. a hyperspectral scanner) that is active on a different wavelength range of the spectrum is recommended to provide better classification results.

BIBLIOGRAPHY

Bartholomeus, H., Clevers, J., & Kooistra, L. (2015). Course reader - GRS-20306 - Remote Sensing . Wageningen: Laboratory of Geo-Information Science and Remote Sensing - Wageningen University.

Berendsen, H. (2004). De vorming van het land: inleiding in de geologie en de geomorfologie. Assen: Uitgeverij Van Gorcum.

Chuvieco, E. (2016). *Fundamentals of Satellite Remote Sensing: An Environmental Approach (Second Edition).* CRC Press.

Clevers, J. (2017). *Lecture - GRS-20306 - Remote Sensing: Optical Remote Sensing.* Wageningen: Laboratory of Geo-Information Science and Remote Sensing - Wageningen University.

Clevers, J. (2017). *Lecture - GRS-20306 - Remote Sensing: Vegetation indices - Statistical Methods.* Wageningen: Laboratory of Geo-Information Science and Remote Sensing - Wageningen University.

Duda, R., & Hart, P. (1973). *Pattern Classification and Scene Analysis.* New York: John Wiley & Sons.

ESRI. (2017, 07 19). *ArcMap*. Retrieved from ArcGIS for Desktop: http://desktop.arcgis.com/en/arcmap/10.3/main/map/what-is-arcmap-.htm

Fugro Engineers B.V. (2015). *Report No. N6083/06 - Geological Ground Model - Wind Farm Site IV Borssele Wind Farm.* Nootdorp: Fugro Engineers B.V.

Hirmas, D. R., Giménez, D., Filho, A. M., Patterson, M., Drager, K., Platt, B. F., & Eck, D. V. (2016). Quantifying Soil Structure and Porosity Using Three-Dimensional Laser Scanning (Chapter 2). In D. R. Hirmas, D. Giménez, A. M. Filho, M. Patterson, K. Drager, B. F. Platt, & D. V. Eck, *Digital Soil Morphometrics* (pp. 19-35). Springer International Publishing Switzerland.

Hunt, G. (1980). Electromagnetic radiation: The communications link in remote sensing. In B. Siegal, & A. Gillespie, *Remote Sensing in Geology* (pp. 5-45). New York: Wiley.

Irons, J., Weismiller, R., & Petersen, G. (1989). Soil Reflectance. In J. Irons, R. Weismiller, & G. Petersen, *Theory and Applications of Optical Remote Sensing* (pp. 66-106). John Wiley and Sons.

ITC. (2012). *The core of GIScience: a systems-based approach.* Enschede: The International Institute for Geo-Information Science and Earth Observation (University of Twente).

Kaufmann, R. K., & Cleveland, C. J. (2008). Environmental science. McGraw-Hill College.

Lay, D. C. (2012). Chapter 6: Orthogonality and Least Squares. In D. C. Lay, *Linear Algebra and Its Applications (4th edition)* (pp. 329-392). Pearson.

Leica Geosystems AG. (n.d.). *Leica ScanStation C10.* Retrieved from Website - Leica Geosystems: https://hds.leica-geosystems.com/downloads123/hds/hds/ScanStation%20C10/brochures-datasheet/Leica_ScanStation_C10_DS_en.pdf

Lindenbergh, R. (2015, May 1). *Lecture - AESB2440 - Geostatistics & Remote Sensing: Least Squares.* Delft: Dept. of Geoscience & Remote Sensing - TU Delft. Retrieved from Blackboard TU Delft: http://blackboard.tudelft.nl

Stoner, E., & Baumgardner, M. (1981). In E. Stoner, & M. Baumgardner, *Characteristic Variations in Reflectance of Surface Soils* (pp. 1161 - 1165). Soil Science Society of America Journal, 45(6).

U.S. Geological Survey. (2006, August 18). *San Francisco Bay Region Geology and Geologic Hazards*. Retrieved from USGS: https://geomaps.wr.usgs.gov

van Alboom, G., Dupont, H., Maertens, J., & Haelterma, K. (2012). *Glauconiethoudende zanden.* Geotechniek, 16(2), 32.

van den Bosch, M. (2015). *Lithostratigraphy of the Oligocene in the Almelo-Winterswijk area, Eastern Netherlands.* Eburon Uitgeverij B.V.

Vosselman, G., & Maas, H.-G. (2010). *Airborne And Terrestial Laser Scanning.*

APPENDICES

A. Chronostratigraphic chart – Tongeren Formation

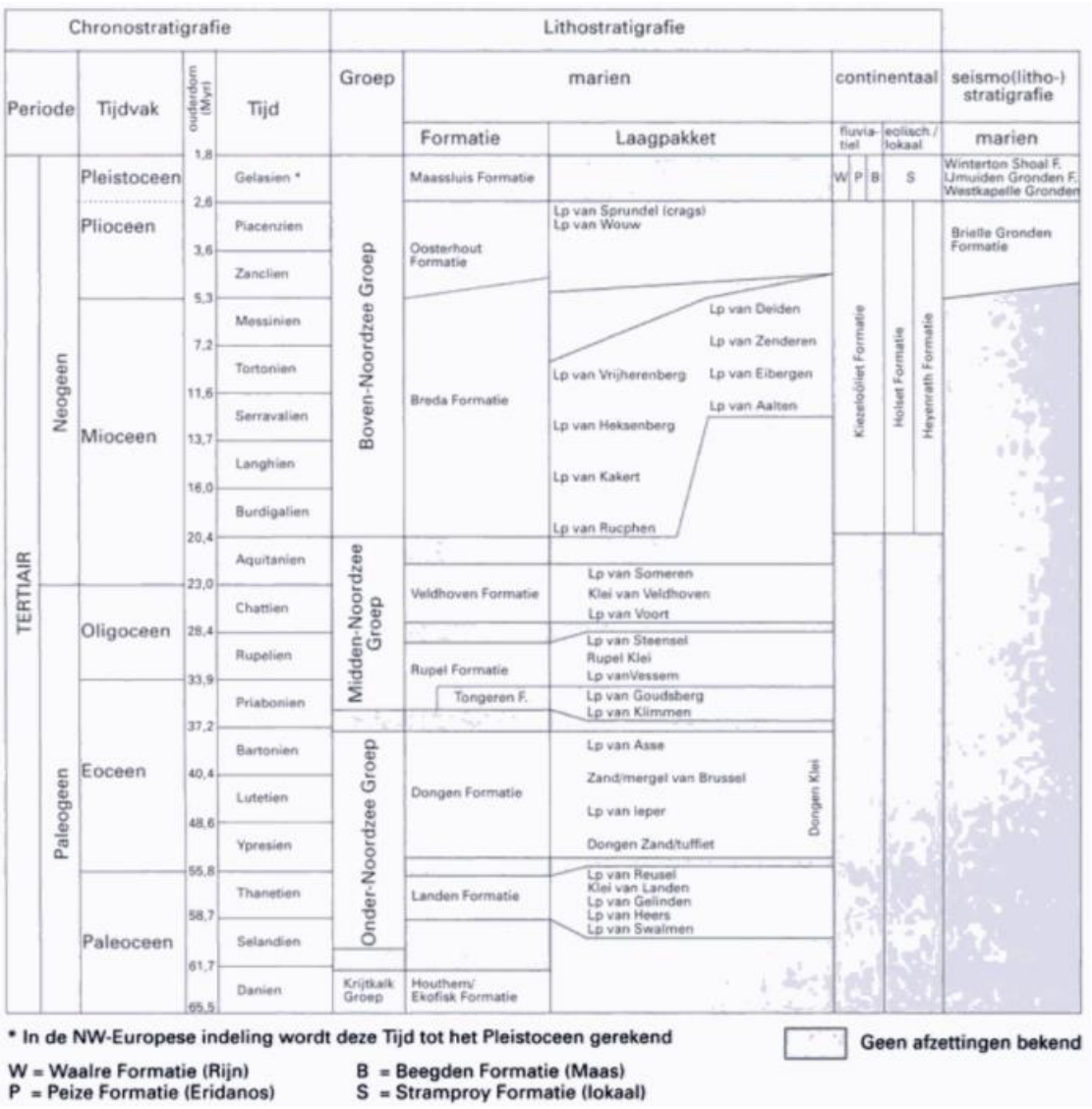

Figure A.1. Chronostratigraphic chart including the Tongeren Formation (Berendsen, 2004).

B. Project material provided by Fugro

i. Borehole B508 – 4

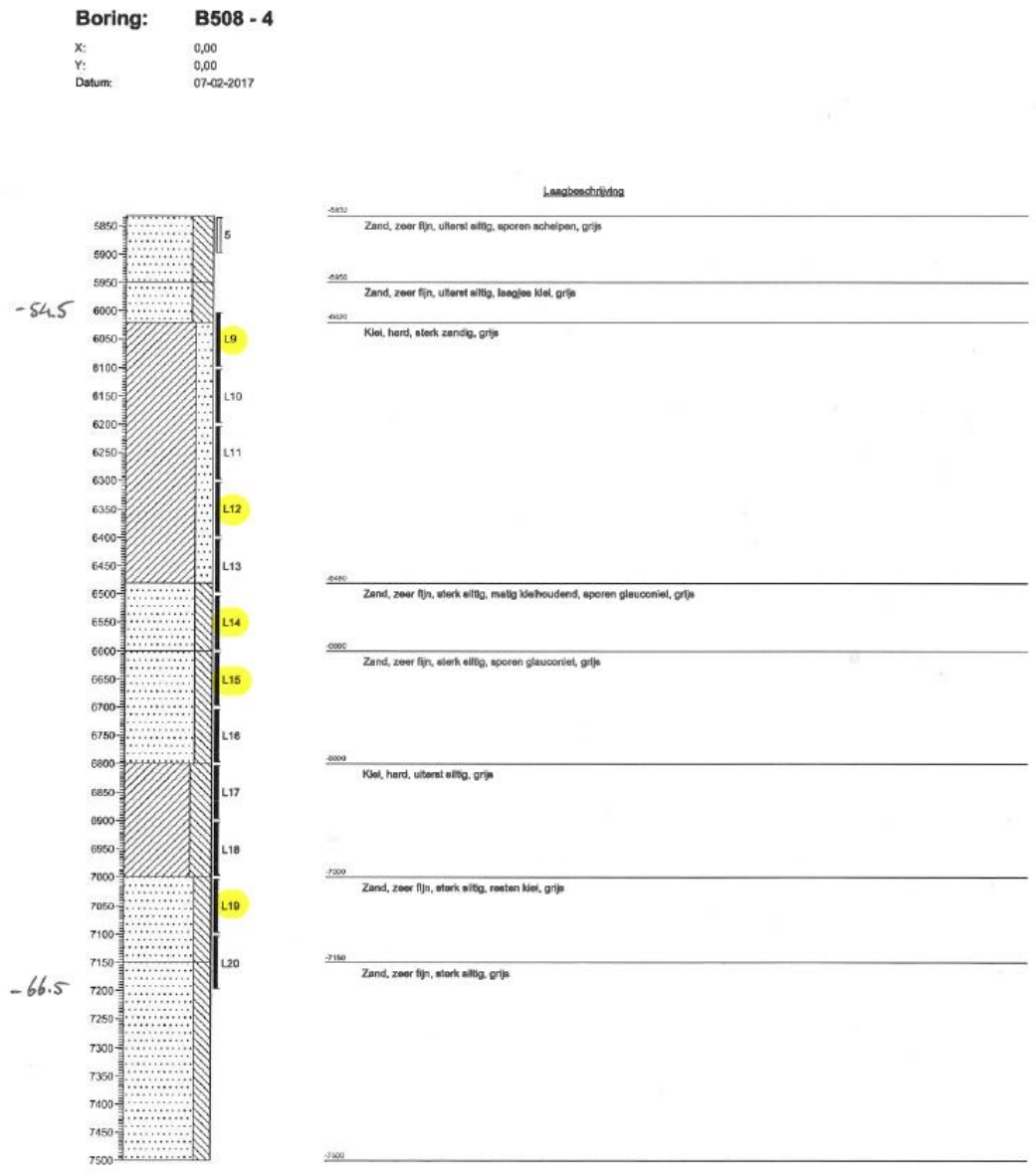

Figure B.1. Cross-section of borehole B508-4. Samples that were provided for the project are L9, L12, L14, L15 and L19, and marked yellow.

ii. Soil descriptions of sample L9, L12, L14, L15 and L19

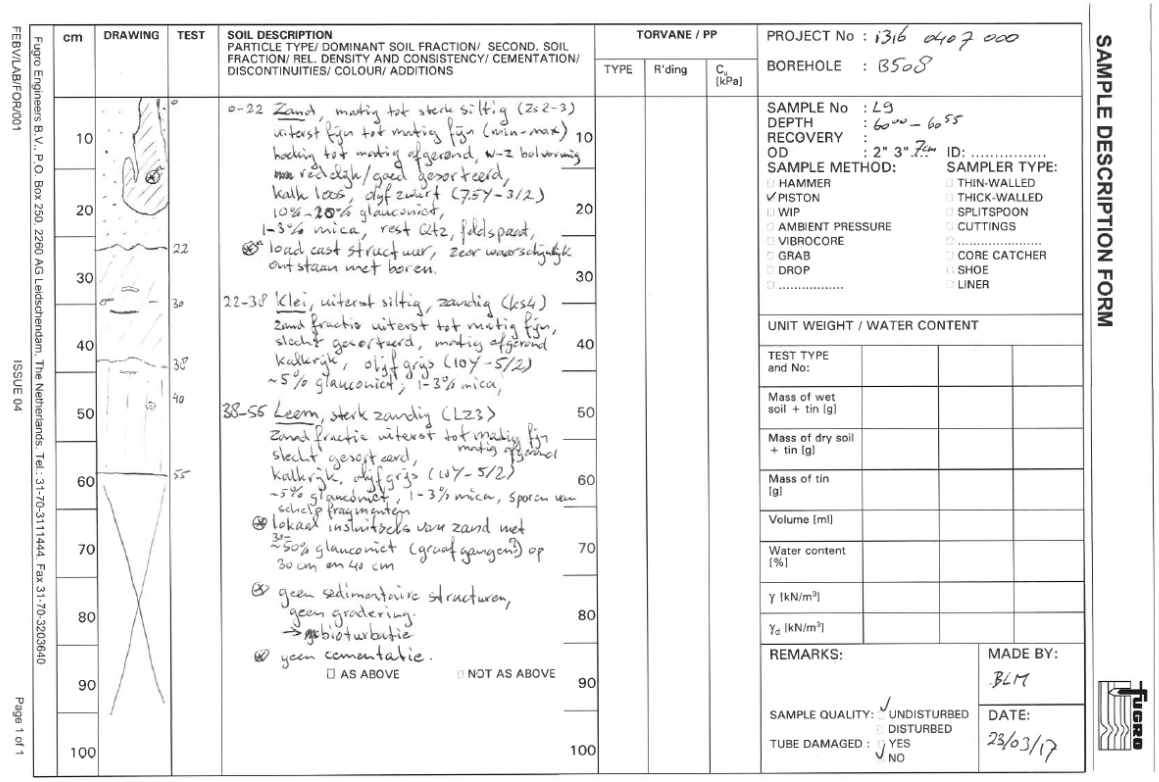

SAMPLE DESCRIPTION FORM

Fugro Engineers B.V., P.O. Box 250, 2260 AG Leidschendam, The Netherlands. Tel.: 31-70-3111444. Fax 31-70-3203640

FEBVLAB/FOR001 ISSUE 04 Page 1 of 1

cm	DRAWING	TEST	SOIL DESCRIPTION (PARTICLE TYPE/ DOMINANT SOIL FRACTION/ SECOND. SOIL FRACTION/ REL. DENSITY AND CONSISTENCY/ CEMENTATION/ DISCONTINUITIES/ COLOUR/ ADDITIONS)	TORVANE / PP TYPE	TORVANE / PP R'ding	TORVANE / PP C_u [kPa]
10		0	0-22 Zand, matig tot sterk siltig (Zs2-3) uiterst fijn tot matig fijn (uiterst-max) hedlig tot matig afgerond, w-z bolvormig matig redelijk/goed gesorteerd, kalkloos, olijfzwart (7.5Y-3/2) 10%-20% glauconiet, 1-3% mica, rest Qtz, veldspaat,			
20		22	load cast structuur, zeer waarschijnlijk ontstaan met boren.			
30		30	22-38 Klei, uiterst siltig, zandig (Ks4) zand fractie uiterst tot matig fijn, slecht gesorteerd, matig afgerond kalkrijk, olijf grijs (10Y-5/2) ~5% glauconiet, 1-3% mica,			
40		38				
50		40	38-55 Leem, sterk zandig (Lz3) zand fractie uiterst tot matig fijn matig afgerond slecht gesorteerd, kalkrijk, olijfgrijs (10Y-5/2) ~5% glauconiet, 1-3% mica, sporen van schelp fragmenten,			
60		55	lokaal insluitsels van zand met ~30-50% glauconiet (graafgangen?) op 30 cm en 40 cm			
70			geen sedimentaire structuren, geen gradering. → bioturbatie			
80			geen cementatie.			
90			☐ AS ABOVE ☐ NOT AS ABOVE			
100						

PROJECT No : 1316 0407 000
BOREHOLE : B508

SAMPLE No : L9
DEPTH : 60.00 – 60.55
RECOVERY :
OD : 2" 3".7cm ID: .....

SAMPLE METHOD: ☐ HAMMER ✓ PISTON ☐ WIP ☐ AMBIENT PRESSURE ☐ VIBROCORE ☐ GRAB ☐ DROP ☐ .....

SAMPLER TYPE: ☐ THIN-WALLED ☐ THICK-WALLED ☐ SPLITSPOON ☐ CUTTINGS ☐ ..... ☐ CORE CATCHER ☐ SHOE ☐ LINER

UNIT WEIGHT / WATER CONTENT

TEST TYPE and No:			
Mass of wet soil + tin [g]			
Mass of dry soil + tin [g]			
Mass of tin [g]			
Volume [ml]			
Water content [%]			
γ [kN/m³]			
γ_d [kN/m³]			

REMARKS:

MADE BY: BLM

SAMPLE QUALITY: ✓ UNDISTURBED ☐ DISTURBED

TUBE DAMAGED : ☐ YES ✓ NO

DATE: 23/03/17

Figure B.2. Sample L9.

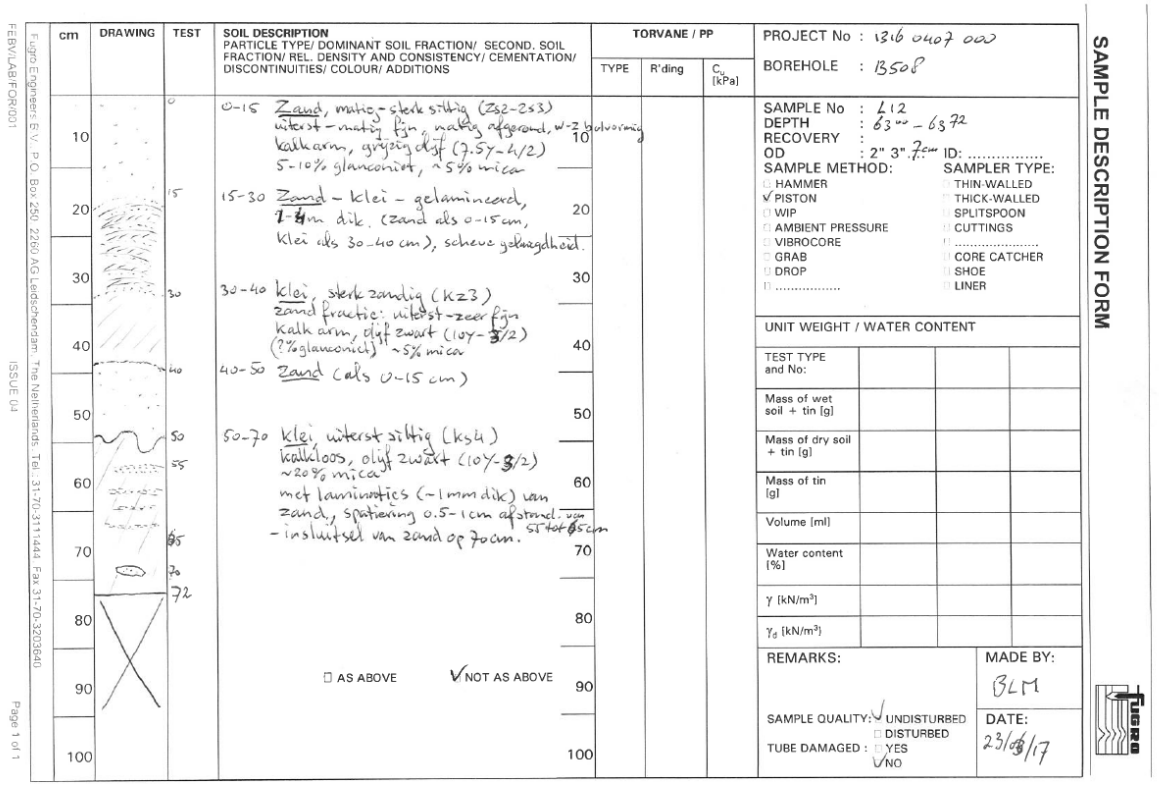

SAMPLE DESCRIPTION FORM

Fugro Engineers B.V., P.O. Box 250, 2260 AG Leidschendam, The Netherlands. Tel.: 31-70-3111444. Fax 31-70-3203640

FEBVLAB/FOR001 ISSUE 04 Page 1 of 1

cm	DRAWING	TEST	SOIL DESCRIPTION (PARTICLE TYPE/ DOMINANT SOIL FRACTION/ SECOND. SOIL FRACTION/ REL. DENSITY AND CONSISTENCY/ CEMENTATION/ DISCONTINUITIES/ COLOUR/ ADDITIONS)	TORVANE / PP TYPE	TORVANE / PP R'ding	TORVANE / PP C_u [kPa]
10		0	0-15 Zand, matig-sterk siltig (Zs2-3s3) uiterst-matig fijn, matig afgerond, w-z bolvormig kalkarm, grijzig olijf (7.5Y-4/2) 5-10% glauconiet, ~5% mica			
20		15	15-30 Zand-klei-gelamineerd, 1-4cm dik. (zand als 0-15cm, klei als 30-40 cm), scherp gelaagdheid.			
30		30	30-40 klei, sterk zandig (Kz3) zand fractie: uiterst-zeer fijn kalkarm, olijf zwart (10Y-3/2) (?% glauconiet) ~5% mica			
40		40	40-50 Zand (als 0-15 cm)			
50		50	50-70 klei, uiterst siltig (Ks4) kalkloos, olijf zwart (10Y-3/2) ~20% mica met laminaties (~1mm dik) van zand, spatiering 0.5-1cm afstand. vanaf 55 tot 65cm - insluitsel van zand op 70cm.			
60		55				
70		65				
80		70 72				
90			☐ AS ABOVE ✓ NOT AS ABOVE			
100						

PROJECT No : 1316 0407 000
BOREHOLE : B508

SAMPLE No : L12
DEPTH : 63.00 – 63.72
RECOVERY :
OD : 2" 3".7cm ID: .....

SAMPLE METHOD: ☐ HAMMER ✓ PISTON ☐ WIP ☐ AMBIENT PRESSURE ☐ VIBROCORE ☐ GRAB ☐ DROP ☐ .....

SAMPLER TYPE: ☐ THIN-WALLED ☐ THICK-WALLED ☐ SPLITSPOON ☐ CUTTINGS ☐ ..... ☐ CORE CATCHER ☐ SHOE ☐ LINER

UNIT WEIGHT / WATER CONTENT

TEST TYPE and No:			
Mass of wet soil + tin [g]			
Mass of dry soil + tin [g]			
Mass of tin [g]			
Volume [ml]			
Water content [%]			
γ [kN/m³]			
γ_d [kN/m³]			

REMARKS:

MADE BY: BLM

SAMPLE QUALITY: ✓ UNDISTURBED ☐ DISTURBED

TUBE DAMAGED : ☐ YES ✓ NO

DATE: 23/03/17

Figure B.3. Sample L12.

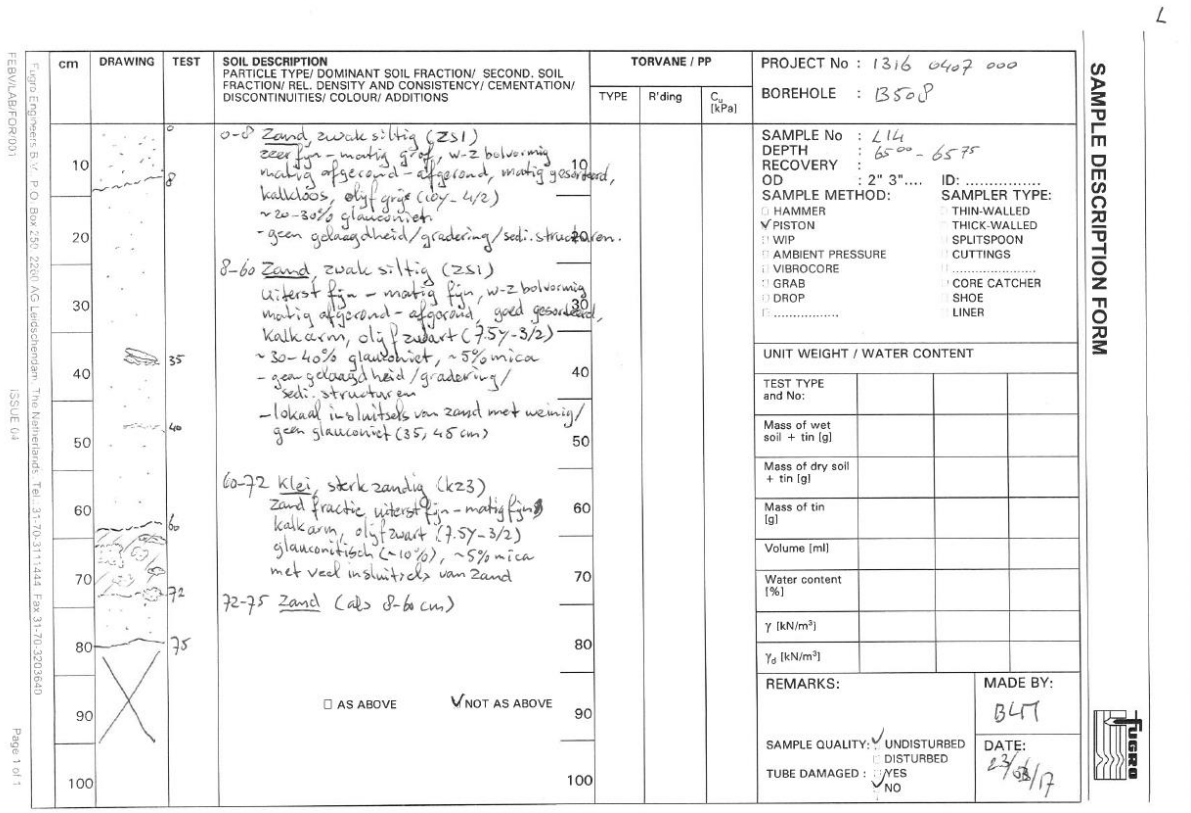

SAMPLE DESCRIPTION FORM

Fugro Engineers B.V. P.O. Box 250, 2260 AG Leidschendam, The Netherlands. Tel. 31-70-3111444. Fax 31-70-3203640

FEBVLAB/FOR/001 ISSUE 04 Page 1 of 1

cm	DRAWING	TEST	SOIL DESCRIPTION (PARTICLE TYPE/ DOMINANT SOIL FRACTION/ SECOND. SOIL FRACTION/ REL. DENSITY AND CONSISTENCY/ CEMENTATION/ DISCONTINUITIES/ COLOUR/ ADDITIONS)	TORVANE / PP: TYPE	TORVANE / PP: R'ding	TORVANE / PP: C_u [kPa]
10		0	0-8 Zand, zwak siltig (zs1) zeer fijn – matig grof, w-z bolvorming matig afgerond – afgerond, matig gesorteerd, kalkloos, olijf grijs (10y-4/2) ~20-30% glauconiet - geen gelaagdheid/gradering/sedi. structuren.			
20		8				
30			8-60 Zand, zwak siltig (zs1) uiterst fijn – matig fijn, w-z bolvorming matig afgerond – afgerond, goed gesorteerd, kalkarm, olijf zwart (7.5y-3/2) ~30-40% glauconiet, ~5% mica - geen gelaagdheid/gradering/ sedi. structuren - lokaal insluitsels van zand met weinig/ geen glauconiet (35, 45 cm)			
40		35				
50		40				
60		60	60-72 Klei, sterk zandig (kz3) zand fractie uiterst fijn – matig fijn kalkarm, olijf zwart (7.5y-3/2) glauconitisch (~10%), ~5% mica met veel insluitsels van zand			
70		72	72-75 Zand (cabs 8-60 cm)			
80		75				
90			☐ AS ABOVE ☑ NOT AS ABOVE			
100						

PROJECT No : 1316 0407 000

BOREHOLE : B508

SAMPLE No : L14
DEPTH : 65.00 - 65.75
RECOVERY :
OD : 2" 3".... ID: .....

SAMPLE METHOD: ☐ HAMMER ☑ PISTON ☐ WIP ☐ AMBIENT PRESSURE ☐ VIBROCORE ☐ GRAB ☐ DROP ☐ .....

SAMPLER TYPE: ☐ THIN-WALLED ☐ THICK-WALLED ☐ SPLITSPOON ☐ CUTTINGS ☐ ..... ☐ CORE CATCHER ☐ SHOE ☐ LINER

UNIT WEIGHT / WATER CONTENT

TEST TYPE and No:			
Mass of wet soil + tin [g]			
Mass of dry soil + tin [g]			
Mass of tin [g]			
Volume [ml]			
Water content [%]			
γ [kN/m³]			
γ_d [kN/m³]			

REMARKS:

MADE BY: BLT

SAMPLE QUALITY: ☑ UNDISTURBED ☐ DISTURBED

TUBE DAMAGED : ☐ YES ☑ NO

DATE: 23/02/17

Figure B.4. Sample L14.

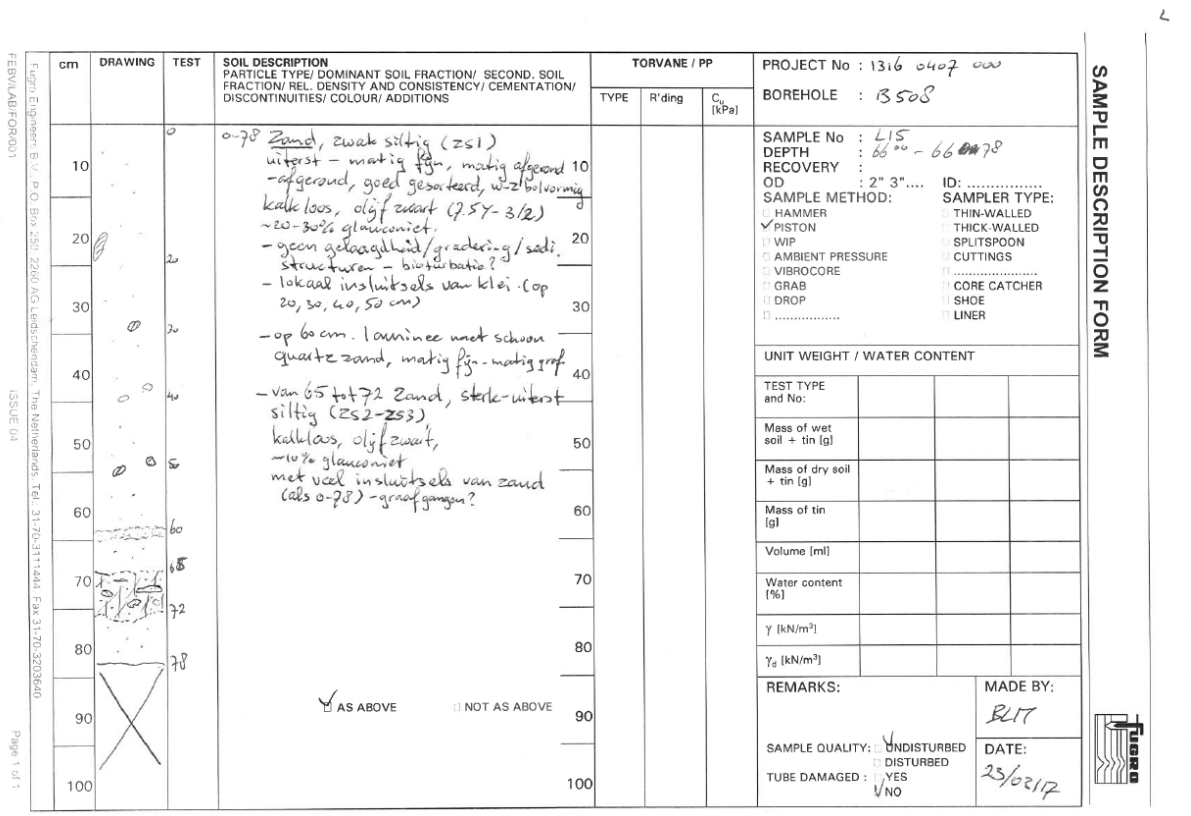

SAMPLE DESCRIPTION FORM

Fugro Engineers B.V. P.O. Box 250, 2260 AG Leidschendam, The Netherlands. Tel. 31-70-3111444. Fax 31-70-3203640

FEBVLAB/FOR/001 ISSUE 04 Page 1 of 1

cm	DRAWING	TEST	SOIL DESCRIPTION (PARTICLE TYPE/ DOMINANT SOIL FRACTION/ SECOND. SOIL FRACTION/ REL. DENSITY AND CONSISTENCY/ CEMENTATION/ DISCONTINUITIES/ COLOUR/ ADDITIONS)	TORVANE / PP: TYPE	TORVANE / PP: R'ding	TORVANE / PP: C_u [kPa]
10		0	0-78 Zand, zwak siltig (zs1) uiterst – matig fijn, matig afgerond – afgerond, goed gesorteerd, w-z bolvorming kalkloos, olijf zwart (7.5y-3/2) ~20-30% glauconiet - geen gelaagdheid/gradering/sedi. structuren – bioturbatie? - lokaal insluitsels van klei (op 20, 30, 40, 50 cm)			
20		20				
30		30				
40		40	- op 60 cm laminae met schoon quartz zand, matig fijn – matig grof			
50		50	- van 65 tot 72 zand, sterk uiterst siltig (zs2-zs3) kalkloos, olijf zwart, ~10% glauconiet met veel insluitsels van zand (cabs 0-78) - graafgangen?			
60		60				
70		72				
80		78				
90			☑ AS ABOVE ☐ NOT AS ABOVE			
100						

PROJECT No : 1316 0407 000

BOREHOLE : B508

SAMPLE No : L15
DEPTH : 66.00 - 66.78
RECOVERY :
OD : 2" 3".... ID: .....

SAMPLE METHOD: ☐ HAMMER ☑ PISTON ☐ WIP ☐ AMBIENT PRESSURE ☐ VIBROCORE ☐ GRAB ☐ DROP ☐ .....

SAMPLER TYPE: ☐ THIN-WALLED ☐ THICK-WALLED ☐ SPLITSPOON ☐ CUTTINGS ☐ ..... ☐ CORE CATCHER ☐ SHOE ☐ LINER

UNIT WEIGHT / WATER CONTENT

TEST TYPE and No:			
Mass of wet soil + tin [g]			
Mass of dry soil + tin [g]			
Mass of tin [g]			
Volume [ml]			
Water content [%]			
γ [kN/m³]			
γ_d [kN/m³]			

REMARKS:

MADE BY: BLT

SAMPLE QUALITY: ☑ UNDISTURBED ☐ DISTURBED

TUBE DAMAGED : ☐ YES ☑ NO

DATE: 23/02/17

Figure B.5. Sample L15.

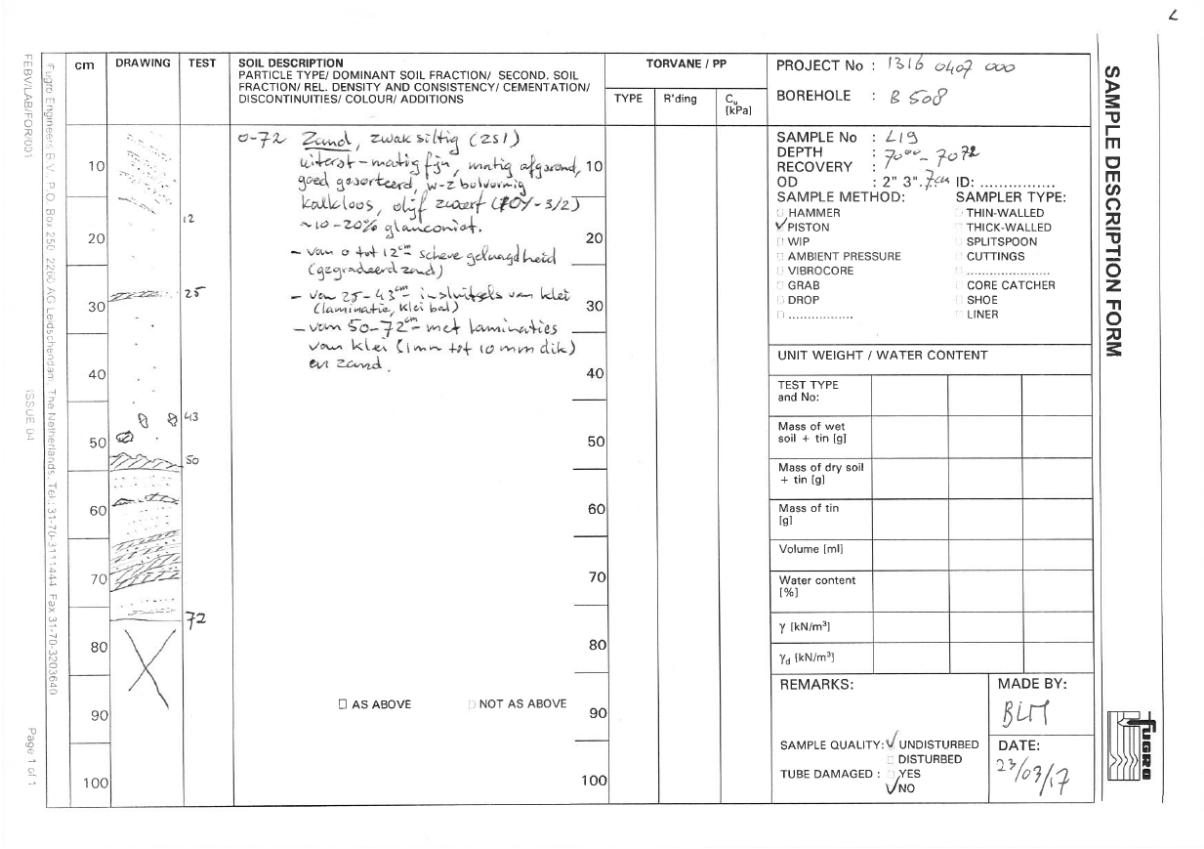

SAMPLE DESCRIPTION FORM

Fugro Engineers B.V. P.O. Box 250, 2260 AG Leidschendam, The Netherlands Tel.: 31-70-311 444 Fax 31-70-3203640

FEBVILAB/FOR/001 ISSUE 04 Page 1 of 1

cm	DRAWING	TEST	SOIL DESCRIPTION PARTICLE TYPE/ DOMINANT SOIL FRACTION/ SECOND. SOIL FRACTION/ REL. DENSITY AND CONSISTENCY/ CEMENTATION/ DISCONTINUITIES/ COLOUR/ ADDITIONS	TORVANE / PP TYPE	R'ding	C_u [kPa]
10			0-72 Zand, zwak siltig (Z51) uiterst – matig fijn, matig afgrond, goed gesorteerd, w-z bolvormig, kalkloos, olijf zwart (5Y-3/2) ~10-20% glauconiet.			
20		12	– van 0 tot 12cm scheve gelaagdheid (gegradeerd zand)			
30		25	– van 25-43cm insluitsels van klei (laminatie, klei bal)			
40			– van 50-72cm met laminaties van klei (1mm tot 10mm dik) en zand.			
50		43 50				
60						
70						
80		72				
90			☐ AS ABOVE ☐ NOT AS ABOVE			
100						

PROJECT No : 1316 0407 000

BOREHOLE : B 508

SAMPLE No : L19
DEPTH : 70.00 - 70.72
RECOVERY :
OD : 2" 3" 7cm ID: .....

SAMPLE METHOD:
☐ HAMMER
☑ PISTON
☐ WIP
☐ AMBIENT PRESSURE
☐ VIBROCORE
☐ GRAB
☐ DROP
☐ .....

SAMPLER TYPE:
☐ THIN-WALLED
☐ THICK-WALLED
☐ SPLITSPOON
☐ CUTTINGS
☐ .....
☐ CORE CATCHER
☐ SHOE
☐ LINER

UNIT WEIGHT / WATER CONTENT

TEST TYPE and No:			
Mass of wet soil + tin [g]			
Mass of dry soil + tin [g]			
Mass of tin [g]			
Volume [ml]			
Water content [%]			
γ [kN/m³]			
γ_d [kN/m³]			

REMARKS:

MADE BY: BLT

SAMPLE QUALITY: ☑ UNDISTURBED ☐ DISTURBED

TUBE DAMAGED : ☐ YES ☑ NO

DATE: 23/07/17

Figure B.6. Sample L19.

iii. Photos of the core samples

Figure B.7. From left to right: L9, L12, L14, L15 and L19. Photo was taken directly after the cutting process.

C. Intermediate results of sample L12 & L14

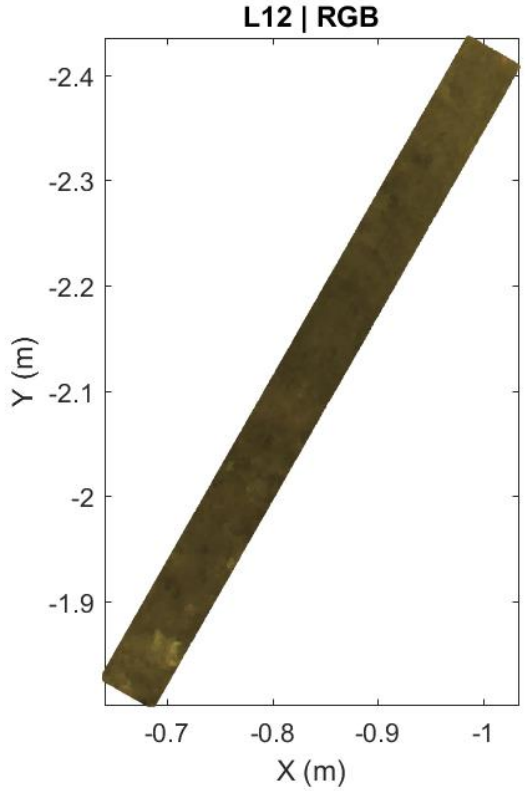

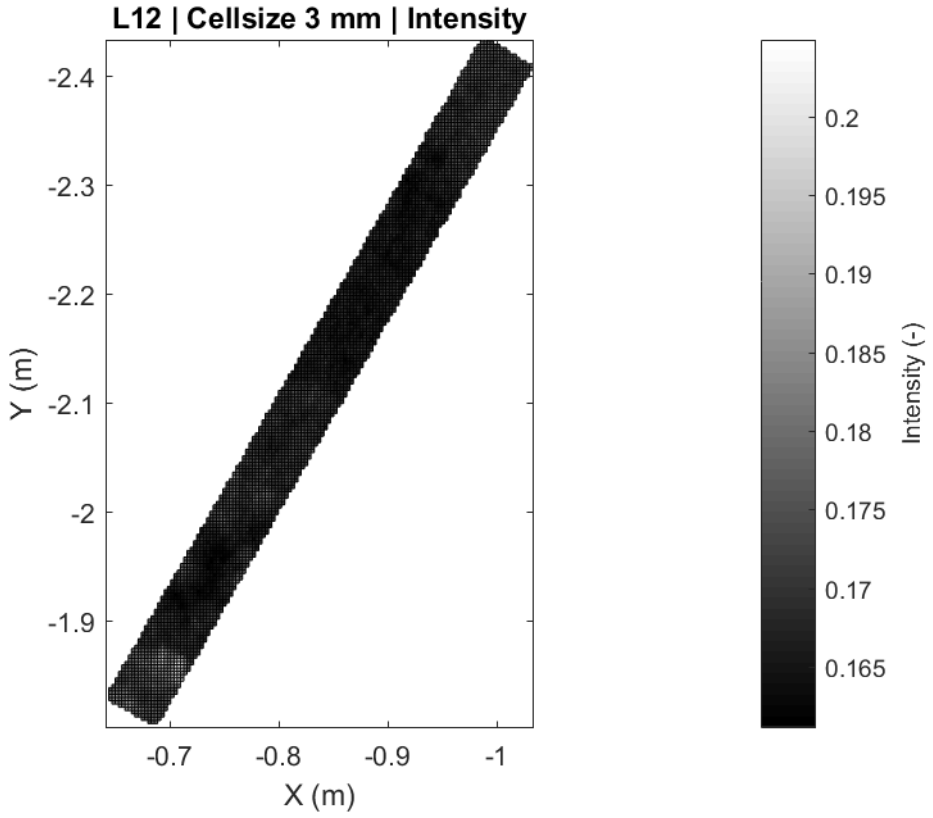

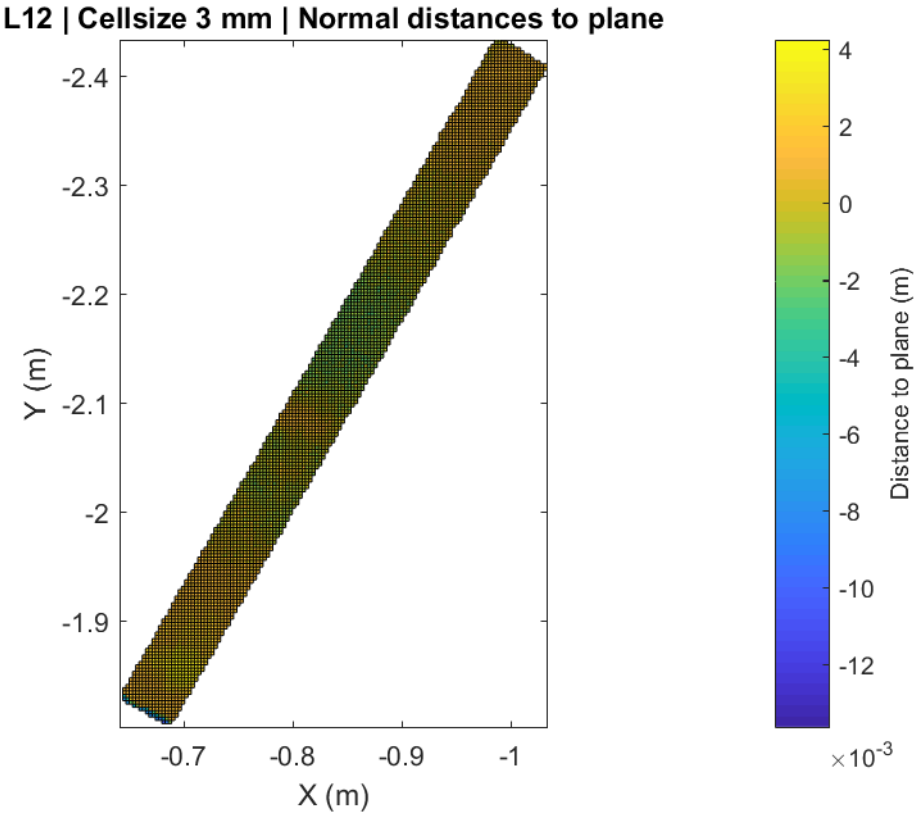
L12 | Cellsize 3 mm | Normal distances to plane
-2.4
-2.3
-2.2
-2.1
-2
-1.9
Y (m)
-0.7
-0.8
-0.9
-1
X (m)
4
2
0
-2
-4
-6
-8
-10
-12
×10-3
Distance to plane (m)

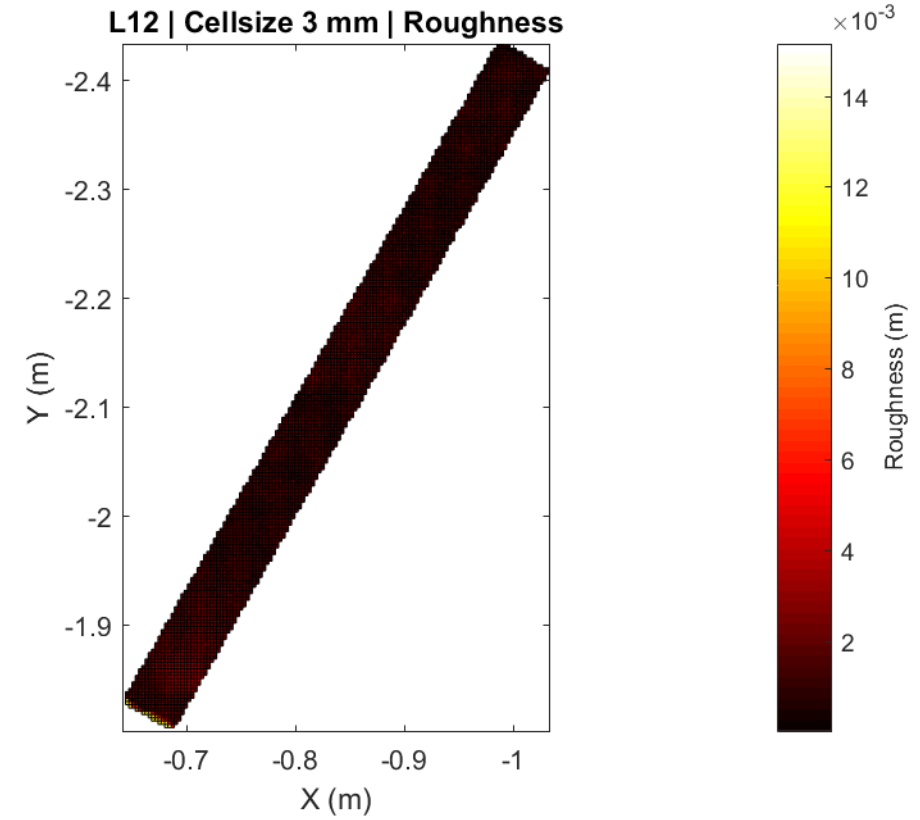
L12 | Cellsize 3 mm | Roughness
-2.4
-2.3
-2.2
-2.1
-2
-1.9
Y (m)
-0.7
-0.8
-0.9
-1
X (m)
×10-3
14
12
10
8
6
4
2
Roughness (m)

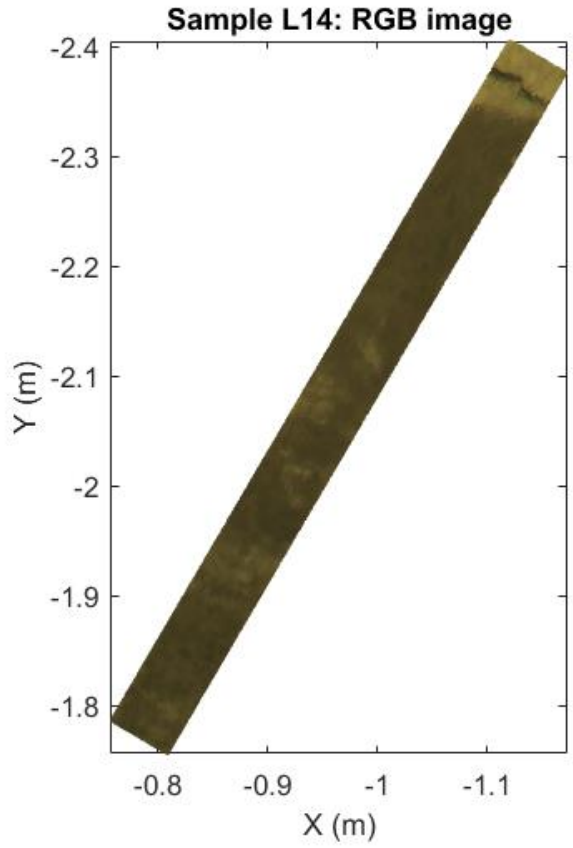
Sample L14: RGB image
-2.4
-2.3
-2.2
-2.1
-2
-1.9
-1.8
Y (m)
-0.8
-0.9
-1
-1.1
X (m)

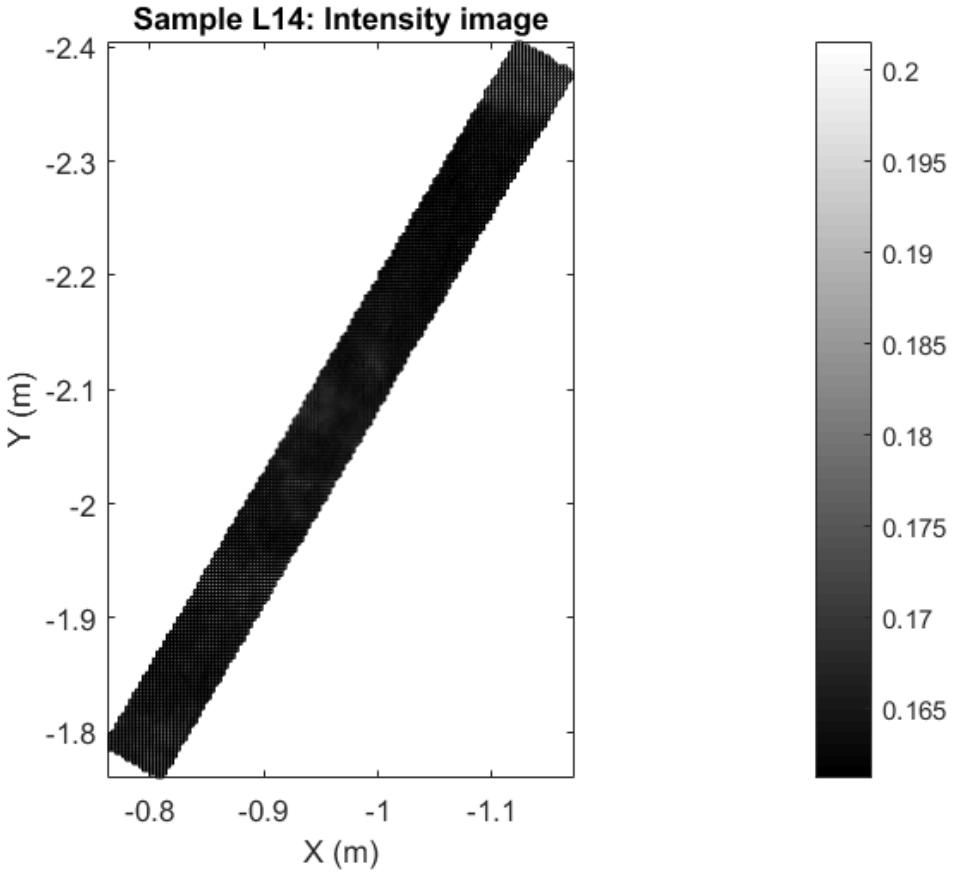
Sample L14: Intensity image
-2.4
-2.3
-2.2
-2.1
-2
-1.9
-1.8
Y (m)
-0.8
-0.9
-1
-1.1
X (m)
0.2
0.195
0.19
0.185
0.18
0.175
0.17
0.165

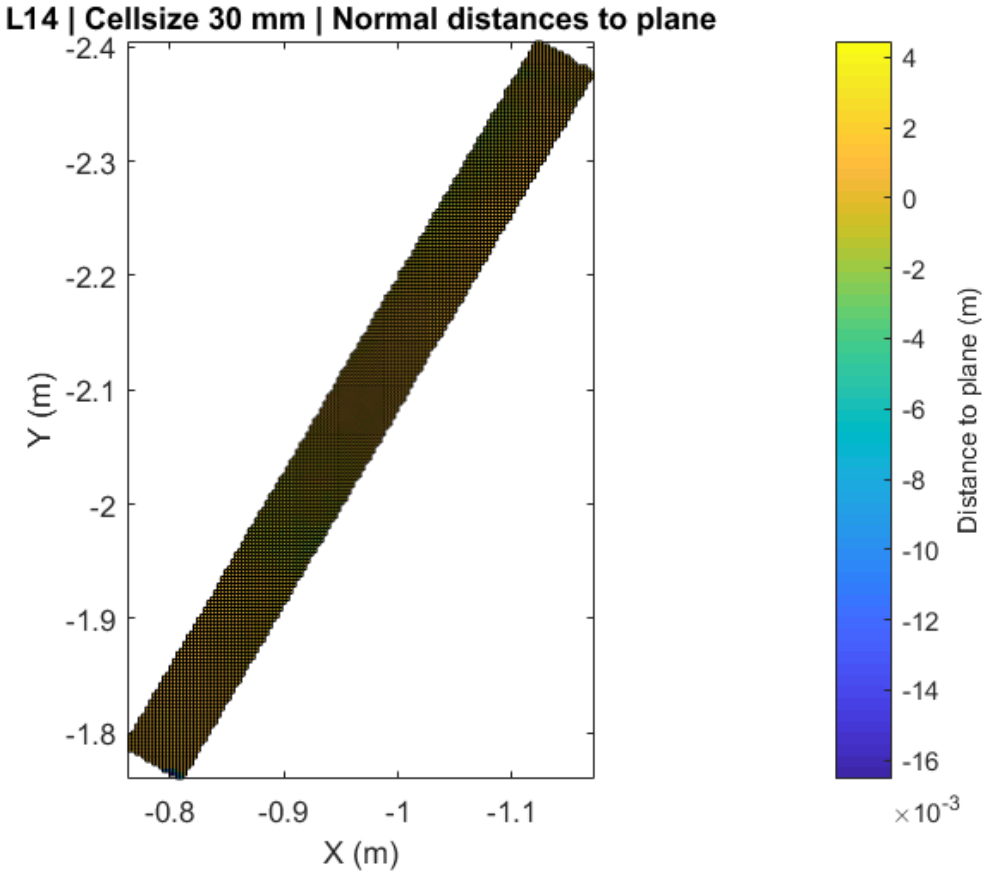
L14 | Cellsize 30 mm | Normal distances to plane
Y (m)
-2.4
-2.3
-2.2
-2.1
-2
-1.9
-1.8
-0.8
-0.9
-1
-1.1
X (m)
Distance to plane (m)
4
2
0
-2
-4
-6
-8
-10
-12
-14
-16
×10-3

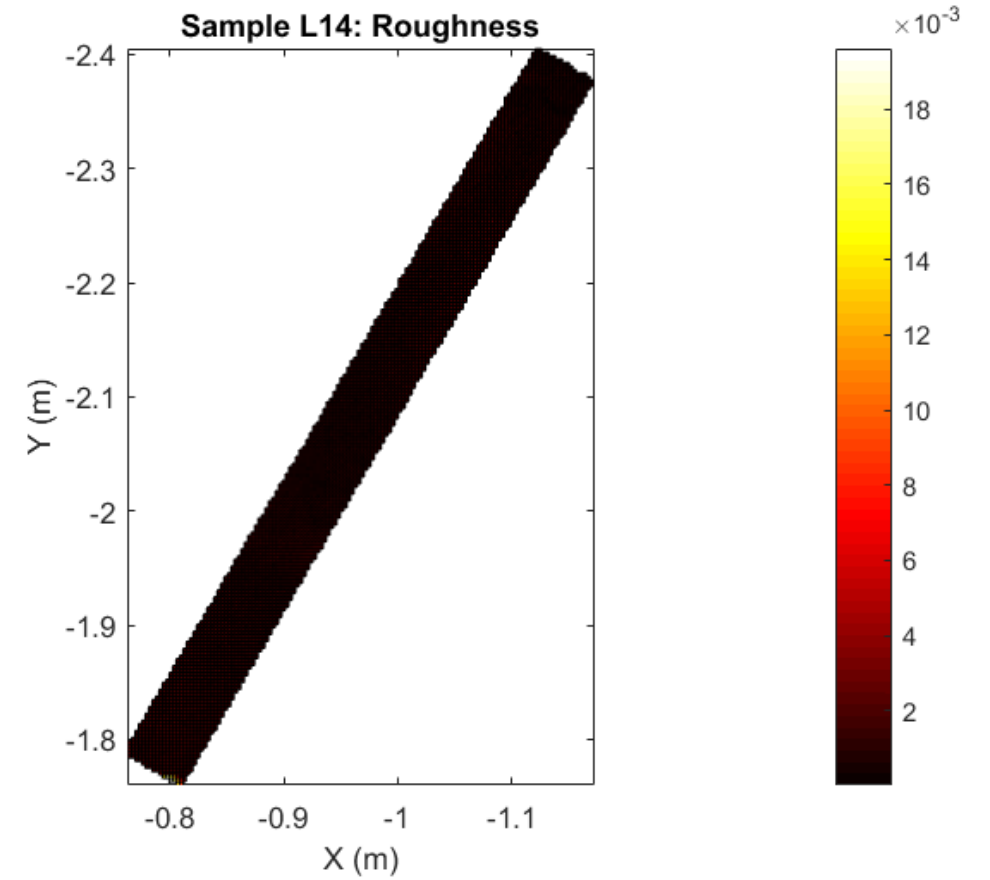
Sample L14: Roughness
Y (m)
-2.4
-2.3
-2.2
-2.1
-2
-1.9
-1.8
-0.8
-0.9
-1
-1.1
X (m)
×10-3
18
16
14
12
10
8
6
4
2

D. Classification results for L9 using different bands

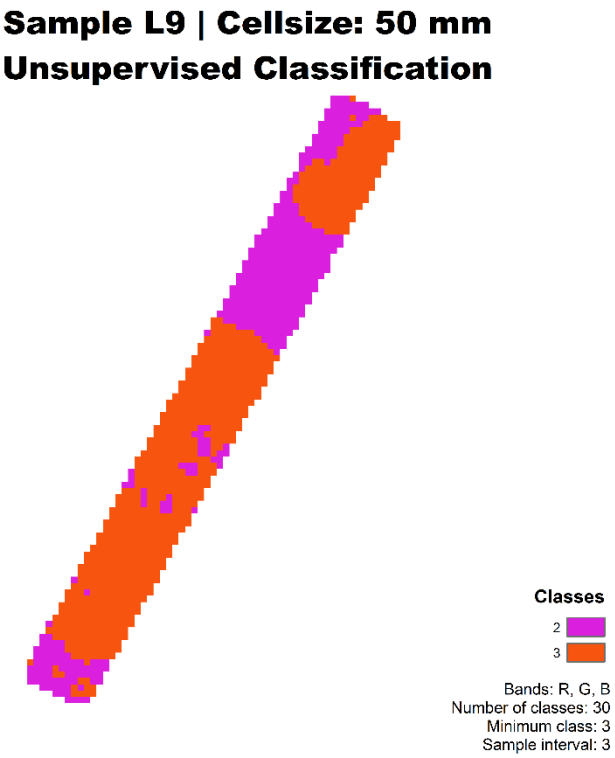

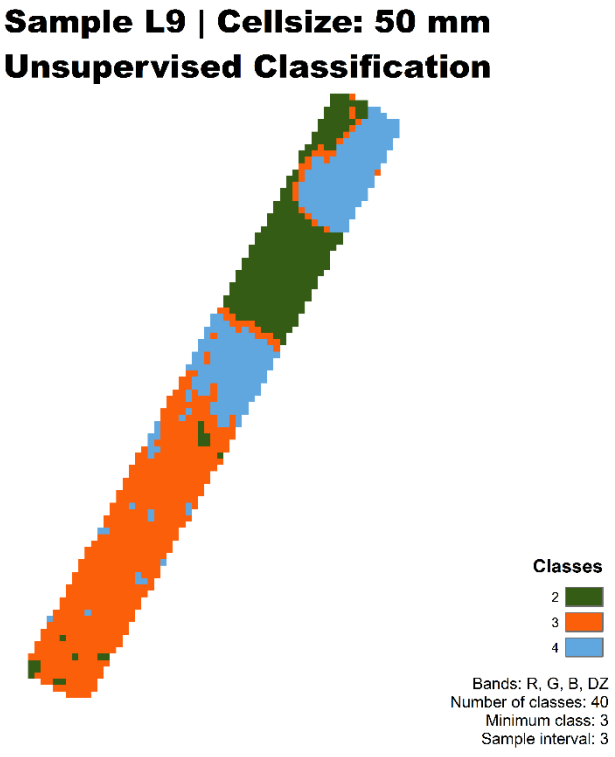

Sample L9 | Cellsize: 50 mm
Unsupervised Classification

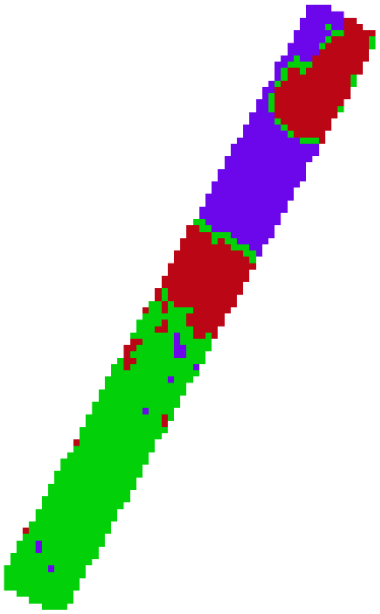

Classes

2
3
4

Bands: R, G, B, I
Number of classes: 40
Minimum class: 3
Sample interval: 3

Sample L9 | Cellsize: 50 mm
Unsupervised Classification

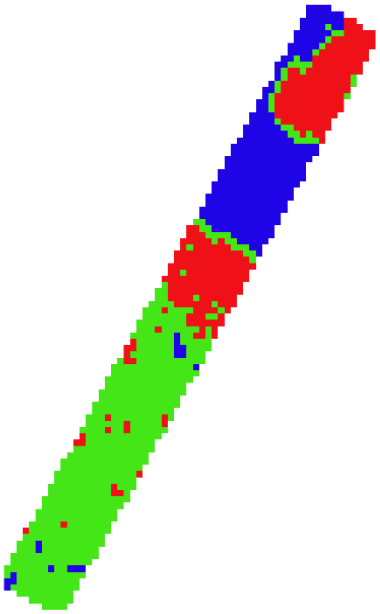

Classes

2
3
4

Bands: R, G, B, RO
Number of classes: 40
Minimum class: 3
Sample interval: 3

E. Matlab code

```
clc
clear all
close all
```

Select appropriate paths

```
addpath(genpath('C:\Users\ivank\Documents\AES\BEP'))
addpath(genpath('C:\Program Files\MATLAB\R2017a\toolbox\vision'))
```

All samples: Read and plot point cloud

```
PC_all =
pcread('C:\Users\ivank\Documents\AES\BEP\ArcMap\workspace\Extra_data\Original\STP2.ply');

figure()
pcshow(PC_all)
title('RGB-image of samples: L9, L12, L14, L15, L19')
xlabel('X (m)')
ylabel('Y (m)')
zlabel('Z (m)')
view([130 90])
```

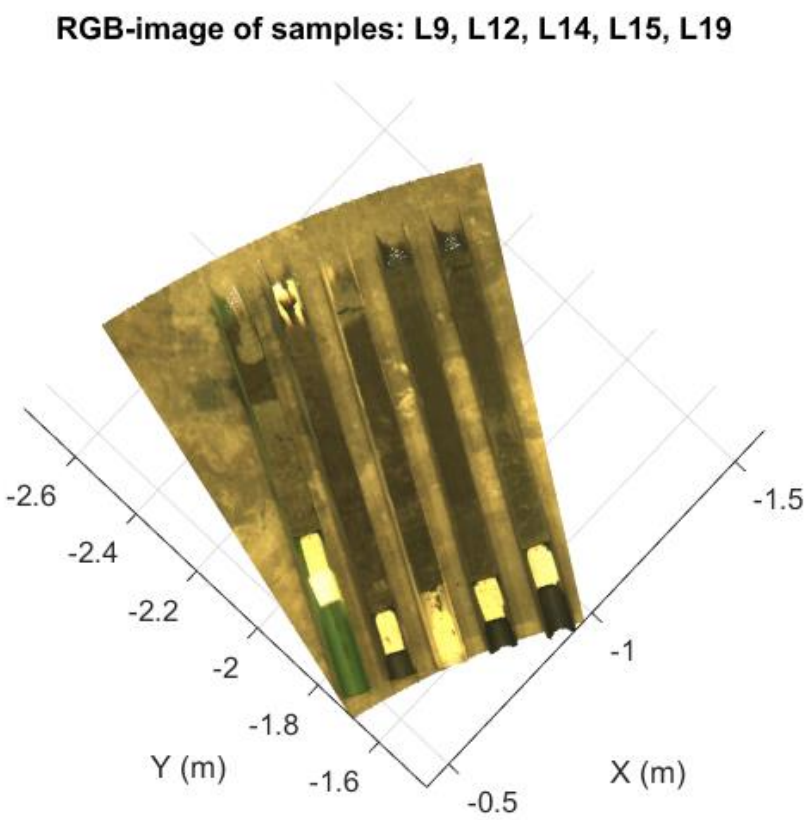

L9: Read point cloud

```
PC_L9 =
pcread('C:\Users\ivank\Documents\AES\BEP\ArcMap\workspace\Extra_data\Original\S1_int_pcd.
pcd');

% PC_L9_Intensity = double(PC_L9.Intensity);%56008x1 matrix single
% PC_L9_XYZ = double(PC_L9.Location);%56008x3 matrix single
PC_L9_RGB = double(PC_L9.Color);%56008x3 matrix uint8
% ptCloud_L9_XYZ = pointCloud(PC_L9_XYZ);

% figure()
% pcshow(PC_L9_XYZ,'MarkerSize',8)
% title('Sample L9: Elevation')
% xlabel('X (m)')
% ylabel('Y (m)')
% zlabel('Z (m)')
% view([180 90])
% colorbar
```

L9: Import Raw Point cloud data from textfile

```
filename =
'C:\Users\ivank\Documents\AES\BEP\ArcMap\workspace\Extra_data\Original\S1.txt';
fileID = fopen(filename,'r');
formatSpec = '%f%f%f%f%f%f%f';
C = textscan(fileID,formatSpec,'Delimiter',',
','EmptyValue',NaN,'Headerlines',0,'MultipleDelimsAsOne',true,'ReturnOnError',1);
X = C{:,1};
Y = C{:,2};
Z = C{:,3};
R = C{:,4};
G = C{:,5};
B = C{:,6};
I = C{:,7};
```

L9: Fitting tool

```
load franke %(only for the first time)
cftool
```

L9: Plane fitting

```
[fitresult, gof] = createFit(X, Y, Z);%Find formula of plane
P1 = fitresult.p00;
P2 = fitresult.p10;
P3 = fitresult.p01;

zplane = zeros(numel(X),1);
zdif = zeros(numel(X),1);
for i = 1:numel(X)
    zplane(i) = P1 + P2*X(i) + P3*Y(i);%y^
    zdif(i) = Z(i) - zplane(i);%e^ = y - y^
end
```

```
% TEST:
% c = ones(numel(X),1);
% A = [X Y c];%model matrix
% x_proj = lscov(A,Z);
```

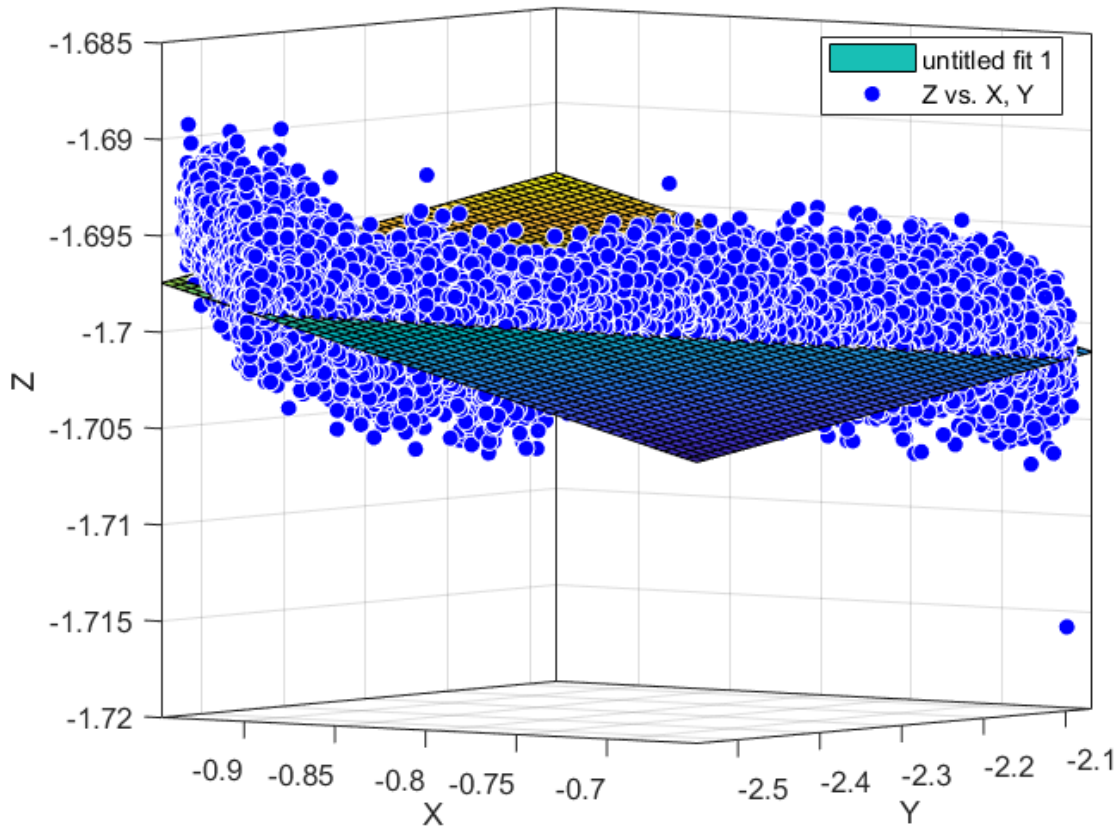

L9: Create table of points (= 1 row) and their features --> FOR METHOD 2

```
L9_table = [X Y Z zplane zdif R G B I];%Unorganised matrix

filename =
'C:\Users\ivank\Documents\AES\BEP\ArcMap\workspace\Extra_data\SampleL9\L9_table.txt';
dlmwrite(filename,[]);%Write empty file
fid = fopen(filename,'wt');
fprintf(fid,'%s\t%s\t%s\t%s\t%s\t%s\t%s\t%s\t%s\n','X','Y','Z','ZPLANE','ZDIF','R','G','B
','I');%Create headers
fclose(fid);
dlmwrite(filename,L9_table,'delimiter','\t','-append');%Add L9_table below headers
```

L9: Construct 3D-matrix (X,Y) with 10 features: nodes(x-array), nodes(y-array),Z,z_plane,z_dif,sigma,R,G,B,I

```
cellsize = 0.0030; %meters
x_array = min(X):cellsize:max(X);
y_array = min(Y):cellsize:max(Y);

L9 = zeros(numel(y_array),numel(x_array),9);
for i = 1:numel(x_array)-1
```

```
    for j = 1:numel(y_array)-1
        % Calculate X-nodes and Y-nodes of each cell
        L9(j,i,1) = (x_array(i)+x_array(i+1))/2;
        L9(j,i,2) = (y_array(i)+y_array(i+1))/2;

        % Find indices of corresponding cell in x and y direction
        [row_x,col_x] = find(X > x_array(i) & X < x_array(i+1));
        [row_y,col_y] = find(Y > y_array(j) & Y < y_array(j+1));
        index = intersect(row_x,row_y);

        % Calculate mean Z(measured) of each cell
        z_mean = mean(Z(index));
        L9(j,i,3) = z_mean;

        % Calculate Z(plane)
        zplane_mean = mean(zplane(index));
        L9(j,i,4) = zplane_mean;

        % Calculate Z(dif) of each cell (difference between plane height
        % and measured height)
        zdif_mean = mean(zdif(index));
        L9(j,i,5) = zdif_mean;

        % Calculate RMS roughness (standard deviation) of each cell = sigma =
sqrt[(e^T*e)/n]
        zdif_1 = zdif(index);%e^
        zdif_T = zdif_1';%e^T
        n = numel(index);%values count in cell
        sigma = sqrt((zdif_T*zdif_1)/n);
        L9(j,i,6) = sigma;

        % Calculate mean R, G and B values of each cell
        R_mean = mean(R(index));
        L9(j,i,7) = R_mean;
        G_mean = mean(G(index));
        L9(j,i,8) = G_mean;
        B_mean = mean(B(index));
        L9(j,i,9) = B_mean;

        % Calculate mean intensity value of cell
        I_mean = mean(I(index));
        L9(j,i,10) = I_mean;
    end
end

% Sub-matrixes of mean values per cell
L9_z = L9(:,:,3);% Z(measured)
L9_zplane = L9(:,:,4);% Z(plane)
L9_zdif = L9(:,:,5);% Z(plane)
L9_rough = L9(:,:,6);% Roughness
L9_red = L9(:,:,7);% Red
L9_green = L9(:,:,8);% Green
L9_blue = L9(:,:,9);% Blue
L9_RGB = cat(3,L9_red,L9_green,L9_blue);% RGB
L9_int = L9(:,:,10);% Intensity
```

L9: Plots of sub-matrices

```
[xx, yy] = meshgrid(x_array,y_array);

% Roughness (RMS) = standard deviation
figure()
surf(xx(1:end-1,1:end-1),yy(1:end-1,1:end-1),L9_rough(1:end-1,1:end-1))
view([180 90])
colormap hot
c = colorbar;
c.Label.String = 'Roughness (m)';
h = title('L9 | Cellsize 30 mm | Roughness');
set(h,'Position',[-0.8,-2.57]);
xlabel('X (m)')
ylabel('Y (m)')
zlabel('Z (m)')
axis equal
xlim([-1 -0.6])
ylim([-2.55 -2.05])
grid off
box on
print('C:\Users\ivank\Documents\AES\BEP\Images\Sample1\Method1\L9_30_Roughness','-dpng')

% Intensity
figure()
surf(xx(1:end-1,1:end-1),yy(1:end-1,1:end-1),L9_int(1:end-1,1:end-1))
h = title('L9 | Cellsize 30 mm | Intensity');
set(h,'Position',[-0.8,-2.57]);
xlabel('X (m)')
ylabel('Y (m)')
zlabel('Z (m)')
axis equal
view([180 90])
colormap gray
c = colorbar;
c.Label.String = 'Intensity (-)';
xlim([-1 -0.6])
ylim([-2.55 -2.05])
grid off
box on
print('C:\Users\ivank\Documents\AES\BEP\Images\Sample1\Method1\L9_30_Intensity','-dpng')

% ZDIF
figure()
surf(xx(1:end-1,1:end-1),yy(1:end-1,1:end-1),L9_zdif(1:end-1,1:end-1))
h = title('L9 | Cellsize 30 mm | Normal distances to plane');
set(h,'Position',[-0.8,-2.57],'FontName','Helvetica');
xlabel('X (m)')
ylabel('Y (m)')
zlabel('Z (m)')
axis equal
view([180 90])
colormap parula
c = colorbar;
c.Label.String = 'Distance to plane (m)';
xlim([-1 -0.6])
ylim([-2.55 -2.05])
```

```
grid off
box on
print('C:\Users\ivank\Documents\AES\BEP\Images\Sample1\Method1\L9_3O_ZDIF','-dpng')

% RGB
figure()
pcshow(PC_L9,'MarkerSize',40)
h = title('L9 | RGB');
set(h,'Position',[-0.8,-2.57],'FontName','Helvetica');
xlabel('X (m)')
ylabel('Y (m)')
zlabel('Z (m)')
view([180 90])
axis equal
xlim([-1 -0.6])
ylim([-2.55 -2.05])
grid off
box on
print('C:\Users\ivank\Documents\AES\BEP\Images\Sample1\Method1\L9_RGB','-dpng')

% L9: Convert to ASCII (.txt)
% First remove all NAN-values from all matrixes before importing to ArcMap
L9_z(isnan(L9_z)) = 0;
L9_zplane(isnan(L9_zplane)) = 0;
L9_zdif(isnan(L9_zdif)) = 0;
L9_rough(isnan(L9_rough)) = 0;
L9_red(isnan(L9_red)) = 0;
L9_green(isnan(L9_green)) = 0;
L9_blue(isnan(L9_blue)) = 0;
L9_int(isnan(L9_int)) = 0;

arcgridwrite('C:\Users\ivank\Documents\AES\BEP\ArcMap\workspace\Extra_data\SampleL9\L9_ro
ugh.asc',x_array,y_array,L9_rough);
arcgridwrite('C:\Users\ivank\Documents\AES\BEP\ArcMap\workspace\Extra_data\SampleL9\L9_z.
asc',x_array,y_array,L9_z);
arcgridwrite('C:\Users\ivank\Documents\AES\BEP\ArcMap\workspace\Extra_data\SampleL9\L9_zd
if.asc',x_array,y_array,L9_zdif);
arcgridwrite('C:\Users\ivank\Documents\AES\BEP\ArcMap\workspace\Extra_data\SampleL9\L9_re
d.asc',x_array,y_array,L9_red);
arcgridwrite('C:\Users\ivank\Documents\AES\BEP\ArcMap\workspace\Extra_data\SampleL9\L9_gr
een.asc',x_array,y_array,L9_green);
arcgridwrite('C:\Users\ivank\Documents\AES\BEP\ArcMap\workspace\Extra_data\SampleL9\L9_bl
ue.asc',x_array,y_array,L9_blue);
arcgridwrite('C:\Users\ivank\Documents\AES\BEP\ArcMap\workspace\Extra_data\SampleL9\L9_in
t.asc',x_array,y_array,L9_int);
```

F. Point cloud properties

Point Cloud	Count	XLimits (m)	YLimits (m)	ZLimits (m)
L9	56,008	[-0.9458 -0.6503]	[-2.5498 -2.0675]	[-1.7157 -1.6893]
L12	93,782	[-1.0336 -0.6384]	[-2.4350 -1.8001]	[-1.7267 -1.6876]
L14	101,143	[-1.1716 -0.7580]	[-2.4048 -1.7566]	[-1.7407 -1.6942]
L15	119,023	[-1.3103 -0.8578]	[-2.3618 -1.6721]	[-1.7335 -1.6980]
L19	100,938	[-1.4196 -1.0045]	[-2.2830 -1.6420]	[-1.7373 -1.6974]

G. ArcMap models